

Document downloaded from:

<http://hdl.handle.net/10251/184835>

This paper must be cited as:

Mohammadi, S.; Moussavi, G.; Shekoohiyan, S.; Marín García, ML.; Bosca Mayans, F.; Giannakis, S. (2021). A continuous-flow catalytic process with natural hematite-alginate beads

for effective water decontamination and disinfection: Peroxymonosulfate activation leading to dominant sulfate radical and minor non-radical pathways. *Chemical Engineering Journal*. 411:1-21.

<https://doi.org/10.1016/j.cej.2020.127738>



The final publication is available at

<https://doi.org/10.1016/j.cej.2020.127738>

Copyright Elsevier

Additional Information

17 **Abstract**

18 A natural, ferruginous soil (HRS) was used as a catalyst for decontamination and disinfection via PMS
19 activation. The HRS was fully characterized (morphological, structural, chemical properties) and was
20 mainly comprised of $\alpha\text{-Fe}_2\text{O}_3$. Complete degradation and 88.6% mineralization of Diclofenac (DCF) was
21 achieved in the HRS/PMS process (10 mg/L HRS, 75 mg/L PMS) within 8 min at neutral pH, while sulfate
22 and chloride did not inhibit the process. *E. coli* and *Enterococcus sp.* were rapidly inactivated in shorter
23 timeframe than DCF. The rapid purification was attributed to $\text{SO}_4^{\bullet-}$, less to $^1\text{O}_2$ and almost insignificant
24 HO^\bullet participation; the degradation mechanisms and transformation pathways were fully elucidated by
25 scavenging tests/EPR, and LC/MS, respectively. With a view in potential applications, HRS was supported
26 on alginate beads (HRSB), maintaining high activity and high reusability (x5 reuse). Finally, a continuous-
27 flow, packed-bed process with HRSB/PMS was assessed, where DCF degradation and mineralization was
28 reached within 2 min HRT.

29

30 **Keywords:** Natural mineral; iron oxide; PMS activation; singlet oxygen; emerging contaminants.

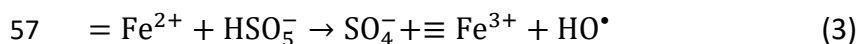
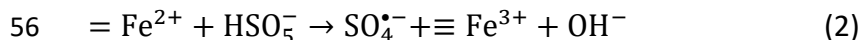
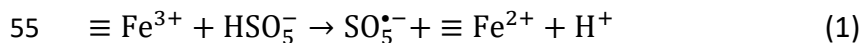
31

32 **1. Introduction**

33 Advanced oxidation processes (AOPs) are efficient processes for the degradation of potentially toxic and
34 biologically recalcitrant organic contaminants. Reactive oxygen species (ROS) such as hydroxyl radical
35 (HO^\bullet), superoxide radical ($\text{O}_2^{\bullet-}$), hydroperoxyl radical (HO_2^\bullet) and singlet oxygen ($^1\text{O}_2$) which can be
36 generated during AOPs treatment are capable of preferentially or non-selectively oxidize and mineralize
37 various organic contaminants (Ma et al., 2019). Besides the aforementioned classic AOPs, sulfate radical
38 AOPs have also gained considerable merit due to their effectiveness. The use of organic peroxides
39 including peroxydisulfate (PDS) and peroxymonosulfate (PMS) as oxidants can induce the generation of
40 $\text{SO}_4^{\bullet-}$. PMS and PDS have intrinsically low reaction rates, but can be activated by various methods
41 including microwave, ultrasound, ultraviolet, heat, alkalis, transition metals and their oxides, electron
42 conduction and carbon-based catalysts (Matzek and Carter, 2016; Wang and Wang, 2018).

43 An efficient application variation is the activation of PMS/PDS by heterogeneous catalysts, due to the
44 ease in their recovery before discharge or reuse. For this purpose, different noble and non-noble metal
45 oxides such as iron oxides, Al_2O_3 , TiO_2 , CuO , ZnO , CeO_2 , etc. have been synthesized and investigated for
46 the heterogeneous activation of PMS/PDS for the degradation of environmental contaminants (Yan et
47 al., 2019; Zhou et al., 2020; Li et al., 2019). Heterogeneous activation of PMS by transition metal(oxides),
48 compared to the homogeneous analogues, are promising alternatives due to the advantageous
49 properties of the oxides, such as low concentration of metal leaching, effective recycling, and stability of
50 their structure during reaction (Zhou et al., 2020). Several reactive species might be generated through
51 PMS activation with heterogeneous metal(oxides) catalysts, including sulfate radical ($\text{SO}_4^{\bullet-}$), hydroxyl
52 radicals (HO^\bullet), and other reactive oxygen species (ROS) such as superoxide ($\text{O}_2^{\bullet-}$) and singlet oxygen

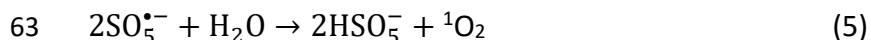
53 ($^1\text{O}_2$). For example, activation of PMS with iron oxides results in the formation of the reactive species
 54 such as HO^\bullet , and $\text{SO}_4^{\bullet-}$, which can be produced through Eqs. (1-3);



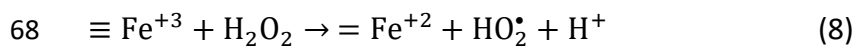
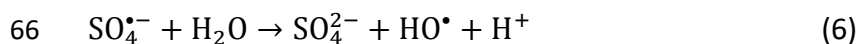
58 In addition, self-decomposition of PMS and the recombination among $\text{SO}_4^{\bullet-}$, $\text{O}_2^{\bullet-}$ and HO_2^\bullet can generate
 59 $^1\text{O}_2$ (Eqs. (4-5)) (Zhou et al., 2020). At alkaline pH, where SO_5^{2-} and HSO_5^- co-exist, we get:



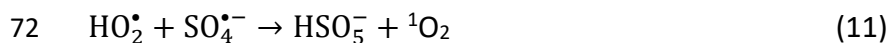
61 While $\text{SO}_5^{\bullet-}$ can oxidize contaminants and bacteria itself (0.84 eV), it can further react with water
 62 molecules to generate $^1\text{O}_2$ (Eq. 5) (Zhou et al., 2020):



64 Also, from the termination reaction of HO^\bullet -radical recombination, H_2O_2 can lead to
 65 superoxide/hydroperoxyl radical:



70 And from hydroperoxyl, radical recombination may result in singlet oxygen generation:



73 Considerable attention has been recently paid on the degradation of organic contaminants in the AOPs
 74 using non-radical reactive oxygen species (ROs) such as $^1\text{O}_2$, although the precise reaction mechanism

75 is evidently complicated and has not established yet (Liu et al., 2018). $^1\text{O}_2$ is a non-radical ROS with
 76 electrophilic nature, which has been largely applied for the oxidation of organic pollutants (Cheng et al.,
 77 2017). The non-radical mechanisms may display substrate-specific reactivity but seems uninvolved to
 78 undesired reactions with background compounds such as natural organic matters (Zhang et al., 2014).
 79 Hence the interest lies in using this pathway to treat wastewaters that may present an inhibition of
 80 radical pathways. However, although factors such as oxygen vacancies lead to non-radical pathways, the
 81 composition of materials may affect the resulting pathways of contaminant elimination. Table 1 presents
 82 some recently published studies on the heterogeneous activation of PMS to evidence the difficulty of
 83 tuning the material to selectively generate $^1\text{O}_2$.

84

85 **Table 1 – PMS activation by natural, metallic and mixed metallic catalysts leading to radical and non-radical**
 86 **pathways.**

Catalyst	Pollutant	Mechanism	Reference
CoFe_2O_4	2,4-dichlorophenol	$\text{SO}_4^{\bullet-}, \text{HO}^\bullet$	(Yang et al., 2009)
$\text{FeCo}_2\text{O}_{4-x}$	2,4-dichlorophenol	$^1\text{O}_2, \text{SO}_4^{\bullet-}, \text{HO}^\bullet$	(Zhou et al., 2020)
$\text{CuFe}_2\text{O}_4/\text{O}_3$	2,4-dichlorophenol	$\text{SO}_4^{\bullet-}, \text{HO}^\bullet, ^1\text{O}_2, \text{O}_2^{\bullet-}$	(Tian et al., 2017)
$\text{CuFe}_2\text{O}_4\text{-Fe}_2\text{O}_3$	Bisphenol A	$\text{SO}_4^{\bullet-}$	(Oh et al., 2015)
MnFe_2O_4	Bisphenol A	$\text{SO}_4^{\bullet-}, \text{HO}^\bullet$	(Deng et al., 2018)
$\text{MnFe}_2\text{O}_4/\text{biochar}$	Orange II	$^1\text{O}_2, \text{SO}_4^{\bullet-}, \text{O}_2^{\bullet-}$	(Fu et al., 2019)
Fe_2O_3	Rhodamine B	$\text{SO}_4^{\bullet-}, \text{HO}^\bullet$	(Ji et al., 2013)
Nano- Fe_2O_3	2,4-dichlorophenol	$\text{SO}_4^{\bullet-}, \text{HO}^\bullet$	(Jaafarzadeh et al., 2017)
Fe_3O_4	Acetaminophen	$\text{SO}_4^{\bullet-}, \text{HO}^\bullet$	(Tan et al., 2014)
$\text{CuOMgO}/\text{Fe}_3\text{O}_4$	4-Chlorophenol	$\text{SO}_4^{\bullet-}, ^1\text{O}_2$	(Jawad et al., 2020)

87

88 For instance, Deng et al. (2018) investigated the degradation of BPA using activation of PMS by MnFe_2O_4
 89 and suggested that the main mechanism is a $\text{SO}_4^{\bullet-}/\text{HO}^\bullet$ radical pathway, however Fu et al. (2019)

90 suggested the induction of further non-radical pathways, due to the porous biochar in the composite.

91 As such, the different PMS activation efficiencies and subsequent degradation driving force obtained by

92 different metal components clearly indicates that the catalytic performance and contaminants'

93 degradation mechanism depend on the source and nature of the catalyst. Also, the need to combine an

94 effective PMS activation, high degradation potential, effectiveness in complex water matrices (natural

95 or wastewater) and easy recovery of a catalyst, are among the key aspects to a successful process.

96 Although some of the materials in Table 1 had notable catalytic activity, due to the complexity, energy-

97 and cost-intensiveness of the synthesizing process, as well as the secondary chemical contamination, the

98 preparation and the application of synthesized materials and nanoparticles raises environmental

99 concerns (Zhang et al., 2020). Using natural materials is an interesting, economically competitive and

100 environmentally benign alternative catalyst choice for the activation of PMS/PDS (Guan et al., 2014). For

101 instance, hematite ($\alpha\text{-Fe}_2\text{O}_3$) is a natural and environmentally friendly catalyst with proven photo-

102 catalytic activity (Demarchis et al., 2015), which is widely distributed and abundant in nature, readily

103 extractable at very low cost. Additionally, it has been shown that doping the iron oxides with the

104 transition metals of Ti, Cr, Mn and Co increased their catalytic activity (Liang et al., 2010); the

105 environmental samples of iron oxides often naturally contain similar "impurities" that lead to enhanced

106 efficacy, albeit in an un-controlled manner.

107 Natural iron (hydr)oxides and minerals, like goethite $\text{FeO}(\text{OH})$, maghemite ($\gamma\text{-Fe}_2\text{O}_3$), ilmenite (FeTiO_3),

108 pyrite (FeS_2) and mackinawite (FeS) are abundant in the Earth's crust. Some of these iron oxides have

109 already been tested as natural catalysts for efficient activation of PDS or PMS for organic contaminants

110 degradation and bacterial inactivation (Xia et al., 2018; Su et al., 2019; Chenxu et al., 2018). For instance,

111 Zhang et al. (2020) investigated the role of a natural bornite (Cu_5FeS_4) as an efficient catalyst for PDS

112 activation for the degradation of tetracycline via HO^\bullet , $\text{SO}_4^{\bullet-}$ and $\text{O}_2^{\bullet-}$. Peng et al. (2020) used a natural
113 chalcopyrite to degrade Bisphenol S, a process that was effectuated via HO^\bullet and $\text{O}_2^{\bullet-}$, while Lai and Lai
114 (2020) degraded atrazine via PMS activation by natural molybdenite to generate HO^\bullet and $\text{SO}_4^{\bullet-}$. Natural
115 materials have also been used in more complex applications such as ultrasound-mediated processes of
116 PMS activation or bio-electro-activation (Diao et al., 2020; Yan et al., 2018).

117 Hence, if the target application is the removal of organic compounds and microorganisms in water, the
118 best option would be i) to use PMS, as a more effective reactive species generator than PDS, ii) apply it
119 in heterogeneous mode in order to avoid metallic sludge and difficulties in catalyst recovery, and iii)
120 intend to use a natural material to minimize the costs associated by synthesizing a material mimicking
121 the natural oxides.

122 In order to meet this multi-level challenge, we considered the use of a natural iron source, Hormuz Red
123 Soil (HRS) as a cheap, available, and environmentally friendly catalyst, used for the first time for the
124 activation of PMS for the degradation of emerging water contaminants and microorganisms. Diclofenac
125 (DCF) was used as a model organic contaminant, while *E. coli* and *Enterococcus sp.* as the bacterial
126 contamination indicators. A full characterization of the morphological, textural and electrochemical
127 properties of HRS was determined, followed by evaluation of the determination of its catalytic activity
128 under different experimental variables, namely the solution pH, catalyst and PMS concentrations,
129 contact time, and water anions in different experimental runs. The reusability and stability of the catalyst
130 was also tested. The type of oxidative species involved in the degradation of DCF in the developed
131 catalytic process was investigated and the degradation mechanism was proposed using the various
132 scavengers. With a view to a potential large-scale application, alginate beads were prepared supporting

133 the HRS powder and the catalytic performance of the system in activating PMS for the degradation of
134 DCF was assessed in batch and in a continuous (flow through) mode with a packed bed column reactor.

135 **2. Materials and methods**

136 **2.1. Chemicals and reagents**

137 Hormuz Red Soil (HRS) was a naturally fine powder, with an abundant source available, extracted from
138 the Hormuz Island (Iran) and used as received without any further purification or processing. The HRS
139 powder was stored in a dark glass and kept in ambient temperature. DCF was obtained from a local
140 pharmaceutical manufacturer as diclofenac sodium powder. Oxone™ (2KHSO₅·KHSO₄·K₂SO₄) was used
141 as the PMS source. The amount of PMS added to the reaction solutions was calculated based on
142 2HSO₅+HSO₄. All the other chemicals used in the present study were of analytical grade and purchased
143 from Sigma-Aldrich, Inc. The solvents used for DCF chromatographic analysis were HPLC-grade. All
144 solutions were prepared with deionized water.

145

146 **2.2. Preparation of the catalyst beads**

147 The catalyst beads were prepared by using sodium alginate following a modified preparation method
148 summarized as follows: 100 g alginic acid sodium salt was dissolved in 100 mL of distilled water and
149 stirred for 30 min at 150 rpm. A 0.2-M CaCl₂ solution was prepared by dissolving a known amount of
150 CaCl₂·2H₂O in distilled a water and used as the beads' hardener solution. A 20-mL suspension of 0.2 g/L
151 HRS was also prepared and sonicated for 30 min at 20 °C. The HRS suspension was then added to the
152 alginate solution and the mixture was stirred for 6 h. The mixture was finally drop-wise added to the
153 hardener solution using a 5-mL plastic syringe and prepare the spherical beads containing the catalyst.
154 The formed beads were kept in the hardener solution for 12 h for proper aging and completing Na⁺/Ca²⁺
155 ion exchange reaction (Wang and Wang, 2018). The beads were then recovered from the solution,

156 washed three times with distilled water and stored in a capped container until used for the treatment
157 experiments. The same procedure was undertaken to prepare the bare beads, during which no catalyst
158 was added to the alginate solution. Supplementary Fig. S1 demonstrates the differences between the
159 prepared beads, i.e. with or without the catalyst. A characterization of the bead morphology showed a
160 spherical shape with an average diameter of 4 ± 0.3 μm .

161

162 **2.3. Material characterization methods and apparatus**

163 The HRS was fully characterized prior to use for its morphological, textural, elemental, and
164 electrochemical properties. The surface morphology was determined by the field emission scanning
165 electron microscopy (FESEM) analysis (FESEM; MIRA3 TESCAN) and the structure of the particles was
166 determined using transmission electron microscopy (TEM; JEOL-2100). The elemental analysis of the
167 catalysts was performed by energy dispersive X-ray (EDX) elemental mapping analysis. Dynamic light
168 scattering (DLS) analysis (Malvern Instruments, Ltd) using water as dispersant was used to measure the
169 size of the catalyst particles. The structural composition was analyzed by X-ray fluorescence (XRF)
170 method on a Philips-X'PERT-PW 2404 instrument. Fourier Transmission Infrared Spectroscopy (FTIR-
171 Thermo Nicolet-Nexus 670) at the wavenumbers ranging from 4000 to 400 cm^{-1} was used to determine
172 the functional groups on surface of the catalyst.

173 The specific surface area of the catalysts was determined based on Brunauer–Emmett–Teller (BET)
174 model from the nitrogen adsorption-desorption isotherms derived at -196 $^{\circ}\text{C}$ using a
175 Micromeritics/Gemini-2372 analyzer. The sample was degassed at 200 $^{\circ}\text{C}$ under vacuum for 2 h before
176 analysis. The crystallinity and phase structure of the powder were analyzed by recording the X-ray
177 diffraction patterns (XRD) at 2θ between 10° and 80° on a Philips X'Pert-MPD X-ray diffractometer

178 operated at 40 kV and 0.04 A with Cu K α radiation at the wavelength of 1.54056 Å. The average crystallite
179 size (d) of iron oxide in the sample was calculated using Debye–Scherrer equation ($d = \frac{0.9 \lambda}{\beta \cos \theta}$) in which
180 λ , β , and θ are the X-ray wavelength, width at half-maximum of the peak, and the position of the peak,
181 respectively. Finally, the binding energies of elements and surface composition of the catalyst were
182 analyzed by X-ray photo-electron spectroscopy (XPS) using a Nicolet spectrometer with an Al-K x-ray
183 source of 1486.6 eV.

184

185 **2.4. Experimental process**

186 The catalytic experiments were conducted in two modes: i) batch experiments for the activation of PMS
187 by HRS (in powder form) or ii) supported HRS by alginate beads in flow-through reactors. In mode I, the
188 activation experiments were conducted using the HRS catalyst in powder form in a glass Erlenmeyer flask
189 as reactor, using a working solution of 100 mL. In a typical reaction, 100 mL of fresh DCF solution was
190 poured into the reactor and mixed by a magnetic stirrer (150 rpm), the required amounts of PMS and
191 HRS were added to the reactor, indicating the beginning of the experiment. The solution was sampled
192 at the time intervals (otherwise noted at a fixed time) and the catalyst was immediately separated from
193 the solution by centrifuging at 5000 rpm during 5 min; the supernatant was filtered through a 0.2 μm
194 cellulose acetate syringe filter, and the filtrate was transferred to labeled vials for target analyses (HPLC).
195 Control tests (blanks) were also conducted under the same procedure in the absence of PMS, as well as
196 of HRS in order to determine the distinct effects of HRS and PMS and the contribution of DCF removal
197 by adsorption to HRS surface or the oxidation with PMS, respectively. Furthermore, the changes in DCF
198 removal in the absence and presence of different scavenging compounds was assessed: tert-butanol

199 (TBA), methanol (MeOH), and Sodium Azide were used as hydroxyl radical (HO^\bullet), sulfate radical ($\text{SO}_4^{\bullet-}$),
200 and singlet oxygen ($^1\text{O}_2$) scavengers, were used to investigate the driving force of DCF degradation.
201 In mode II, a set of experiments was conducted using the catalyst beads under both batch and continuous
202 column test. For the batch tests, 5 spheres of the prepared HRS beads (HRSB) were added to 50 mL of
203 DCF solution (50 mg/L) and the process was run in the presence of 75 mg/L PMS (HRSB/PMS process).
204 The solution was sampled over pre-defined time intervals and the samples were analyzed for their
205 residual DCF. The control experiment was also conducted using the bare beads under similar conditions
206 (bare alginate beads). Continuous flow column tests were also conducted to evaluate the field
207 applicability of the HRSB/PMS process. The schematic setup of the packed bed reactor is given in
208 Supplementary Fig. S2. The total volume of the column was 5 mL and HRSB packed bed volume was 4
209 mL (15 spheres). The fresh DCF solution (50 mg/L) supplemented with 100 mg/L PMS was transferred to
210 the inlet tank. The solution was pumped to the reactor at the bottom at different flow rates, resulting to
211 distinct hydraulic retention times (HRT) ranging from 0.5 to 2 min. At each HRT, the effluent was
212 recovered, and the samples were analyzed for their residual DCF content.

213

214 **2.5. Microbial methods**

215 The *Escherichia coli* and *Enterococcus sp.* used for this study are wildtype strains, natural isolates from
216 secondary wastewater, via selection by Tergitol and Slanetz-Bartley selective Agars, respectively. The
217 use of the specific two model isolates provides a good simulation for the actual bacterial gram-negative
218 and gram-positive pathogens in natural waters/wastewater. Following a successive selection process in
219 proper culture media, the isolated strains were grown overnight in Luria-Bertani (LB) broth and
220 cryogenically stored at -80°C in a 80:20 glycerol:water solution. The process of bacterial growth and

221 strain preparation was published elsewhere in detail (Giannakis et al., 2013). Briefly, a bacterial colony
222 was grown overnight in 10 mL of LB solution under aerobic conditions and agitation (200 rpm) at 37°C,
223 in order to reach stationary phase ($OD_{600}=3-5.5$). Prior to experimentation, the grown culture was
224 centrifuged (2 min at 10.000 rpm) and washed with a sterile saline solution (0.8% NaCl, 0.08% KCl). The
225 OD_{600} of the spiked solution was set to 0.002-0.003 that corresponds to approx. 10^6 CFU/mL.
226 At pre-defined time intervals, 1-mL was recovered from the experiment solution and immediately plated
227 in 9-cm petri dishes containing Plate Count Agar (PCA, Sigma-Aldrich) for *E. coli* or Slanetz-Bartley Agar
228 (SBA, Panreac) for *Enterococcus sp.* Enumeration was performed by applying the spread plate method;
229 0.1 mL of sample was uniformly distributed by 4-mm glass beads, and the plates were incubated for 24
230 or 48 h at 37 °C before enumeration of *E. coli* and *Enterococcus sp.*, respectively. Experiments were
231 performed at least two times (biological replicates), minimum in duplicate (statistical replicates) and
232 plating at least two consecutive aliquots (technical replicates). The presented values represent the
233 average of all the aforementioned tests and the vertical bars indicate standard deviation from the mean.

234

235 **2.6. Analytical methods**

236 The concentration of DCF was determined by a high-performance liquid chromatograph (HPLC, Agilent:
237 1260 infinity Co.) with a UV detector coupled with a reversed-phase C18 separation column (Eclipse plus
238 C18 column; 3.5 μ m, 4.6 mm \times 250 mm). The HPLC was run under the following conditions: sample
239 injection volume = 30 μ L, mobile phase = methanol/phosphate buffer (70/30) mixture, flow rate of 1
240 mL/min, detection wavelength = 264 nm, resulting in a retention time = within 15 min. The concentration
241 of total organic carbon (TOC) was measured with a TOC analyzer (Shimadzu, TOC analyzer –VCSH model).
242 The appropriate standard methods (APHA, 2017) were used for measuring the concentrations of

243 nitrogen species, including ammonium (4500-NH₃-F), nitrite (4500-NO₂⁻-B), nitrate (4500- NO₃⁻-B), and
244 organic nitrogen (4500-Norg-C). The aqueous concentrations of Fe(II) and Fe(III) were determined using
245 a Shimadzu atomic absorption spectrophotometer (Model AA-6200, Japan). The intermediates formed
246 during the degradation of DCF in the developed process under optimum conditions were analyzed using
247 liquid chromatography/mass spectroscopy (LC/MS; Waters Alliance 2695 HPLC-Micromass Quattro
248 micro API mass spectrometer) in both negative and positive electrospray modes. The LC/MS instrument
249 was equipped with an Atlantis T3-C18 3μ column (2.1×100 mm). The mobile phase was a mixture of
250 acetonitrile, water, and 0.1% formic acid injected at the flow rate of 0.25 mL/min.

251

252 **2.7. Electron paramagnetic resonance (EPR) assays details**

253 The EPR measurements were performed in a Wildman Suprasil/aqueous quartz ware flat cell (volume of
254 150 μL, 60 mm of length) with a Bruker EMX 10/12 EPR spectrometer, using the following experimental
255 conditions: microwave power, 20 mW; modulation amplitude, 1.0 G; and modulation frequency, 100
256 kHz. TEMP (2,2,6,6-tetramethylpiperidine) was from Aldrich and 5,5-dimethyl-1-pyrroline-*N*-oxide
257 (DMPO) was from TCI Europe and both were used as received.

258 EPR experiments conducted in the presence of TEMP (100 mM) were carried out in D₂O. Thereby,
259 initially, an aerated mixture of PMS (75 mg/L), HRS (10 mg/L) and TEMP (100 mM) was stirred for 30
260 minutes. Afterwards, the sample was purged with N₂ and submitted to EPR. Reference samples of TEMP
261 100 mM with and without PMS 75 mg/L or HRS (10 mg/L) in aerated D₂O were also analyzed under N₂.

262 The experiments with DMPO (100 mM) were also carried out with PMS (75 mg/L) and HRS (10 mg/L) in
263 aqueous medium. In this case, the reference samples were DMPO (100 mM) with and without PMS 75

264 mg/L or HRS (10 mg/L) in H₂O. These samples were stirred for one minute and then purged with N₂
265 before to submit to the EPR experiment

266

267 **2.8. Performance indices and statistical evaluation**

268 The performance of the developed process was evaluated based on the DCF and TOC removal
269 percentages (Eqs. 12 and 13) and kinetics (Eq. 14). DCF and TOC removals were regarded as the
270 degradation and mineralization percentages.

$$271 \text{ DCF removal (\%)} = \frac{\text{DCF}_0 - \text{DCF}_t}{\text{DCF}_0} \times 100 \quad (12)$$

$$272 \text{ TOC removal (\%)} = \frac{\text{TOC}_0 - \text{TOC}_t}{\text{TOC}_0} \times 100 \quad (13)$$

$$273 \ln \frac{C_t}{C_0} = -k_{\text{obs}}t \quad (14)$$

274 In Eqs. (12 and 13), DCF₀ (TOC₀) and DCF_t (TOC_t) are concentrations of DCF (TOC) at the initial and
275 time t of the reaction, respectively. In Eq. (14), C represents the concentration of DCF or TOC, and k_{obs}
276 indicates the pseudo first order reaction rate constant. For the bacterial tests, the logarithm of the colony
277 forming units per mL (logCFU/mL) are plotted over time. Finally, the calculation of synergy within the
278 involved processes was calculated according to the following equation (Eq. 15):

$$279 S = \frac{k_{12}}{k_1 + k_2} \quad (15)$$

280 Values of synergy S > 1 indicate a synergy among any actions 1 and 2, while S < 1 shows an antagonistic
281 effect.

282 3. Results and discussion

283 3.1. Catalyst characterization

284 The composition of HRS was analyzed using X-ray fluorescence (XRF) technique, and the results are
285 presented in Table 2. The results revealed that HRS contained high amounts of hematite or α -Fe₂O₃
286 (59.30%) and SiO₂ (16.72%), along with a low percentage of organics, determined by the Loss On Ignition
287 test -LOI (6.69%), SO₃ (5.23%), Al₂O₃ (3.76%), and other compounds (8.3%). On the other hand, 76.02%
288 of the total weight percent of HRS was composed of α -Fe₂O₃ and SiO₂ with a Fe/Si ratio of 3.5, and the
289 red color of Hormuz sand is attributed to a high content of iron. The 6.69% value of LOI indicates that
290 the organic content of the catalyst is low. Literature suggests that the presence of SiO₂ and Al₂O₃ in the
291 structure of the catalyst might actually reduce the apparent activation energy of Fe₂O₃ which in turn may
292 result in enhancing its catalytic activity (Gupta et al., 2016). In addition, the presence of silica within the
293 iron catalyst controls the reducibility of Fe₂O₃ in the reaction, due to the surface variations induced to
294 HRS and interaction between iron and silica (Zhang et al., 2006).

295

296 **Table 2. Chemical composition of HRS (wt %).**

Compound	α -Fe ₂ O ₃	SiO ₂	SO ₃	Al ₂ O ₃	MgO	Cl	Na ₂ O	K ₂ O	MnO	L.O.I.	Others
wt%	59.30	16.72	5.23	3.76	1.36	1.06	0.92	0.86	0.17	6.69	3.93

297

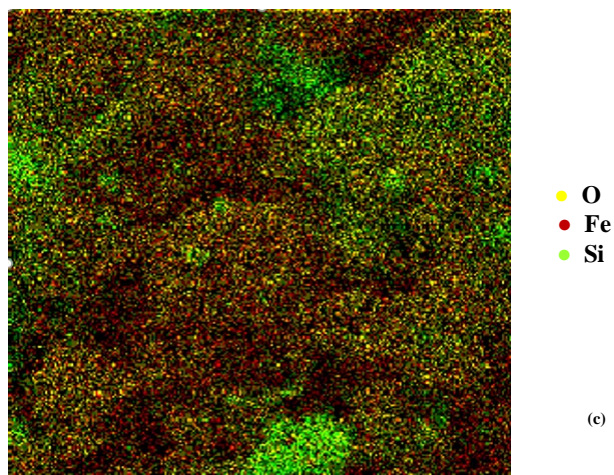
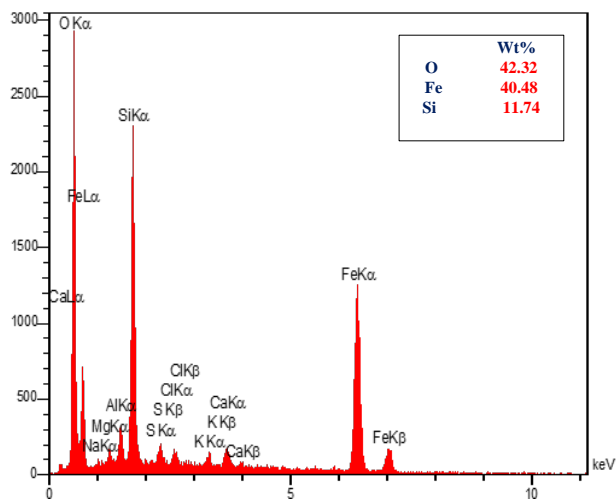
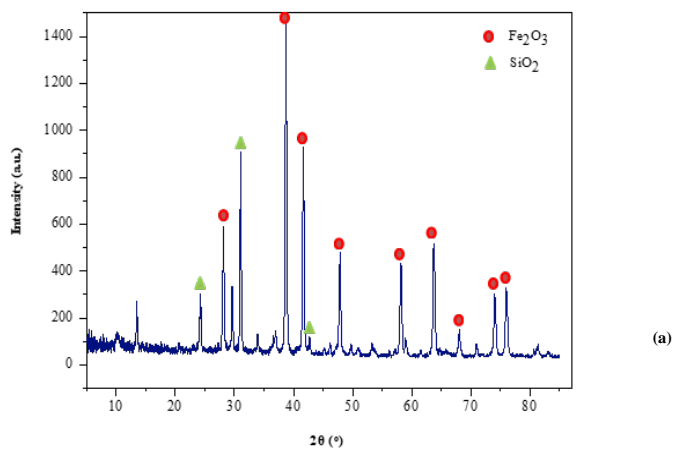
298 The phase purity and crystalline size of HRS before PMS activation were evaluated using XRD analysis.

299 Fig. 1 presents the XRD patterns of fresh (Fig. 1a) HRS sample. The XRD patterns revealed that the

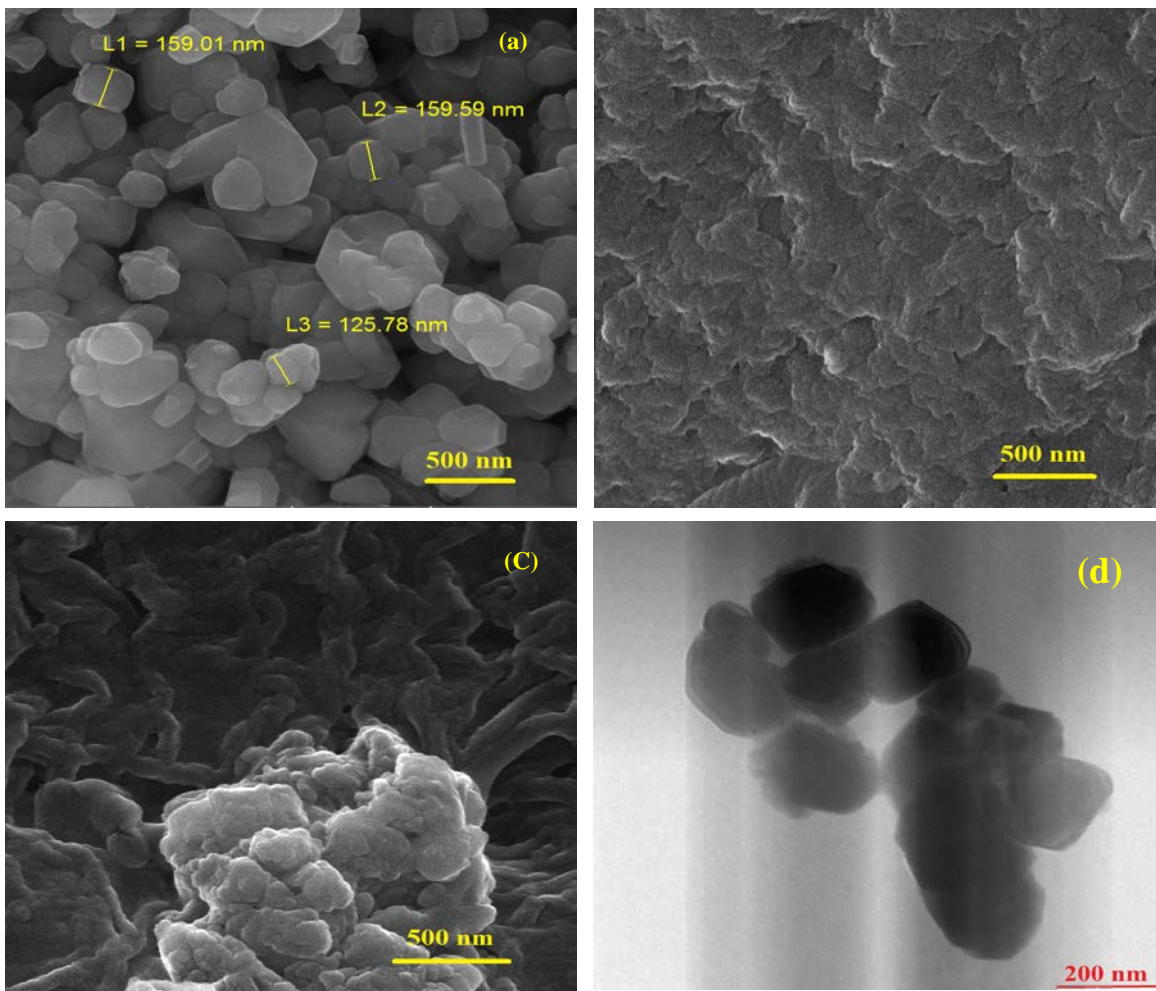
300 principal constituents of the HRS are α -Fe₂O₃ and SiO₂, which is in accordance with the XRF results. Based
301 on JPCDS card No. 79-1741, the sharp and distinctive diffraction peaks appearing at 2 θ of 28.1, 38.7,
302 41.6, 47.83, 58.1, 63.7, 67.9, 74 and 75.9° can be attributed to the 012, 104, 110, 113, 024, 116, 122, 214
303 and 300 planes, confirming that the existence of crystalline particles of Fe₂O₃ in HRS catalyst. All
304 diffraction patterns were in agreement with the phase of hematite (α -Fe₂O₃) reported by other
305 researchers (Yu et al., 2018). The narrow sharp peaks of α -Fe₂O₃ indicate that the structure of hematite
306 is highly crystalline with low impurities (Lassoued et al., 2017). The diffraction peaks for SiO₂ were
307 matched with the JCPDS No. 58-0796 and the diffraction peaks at 2 θ of 24.3, 31.07 and 42.7° were
308 assigned to SiO₂. In addition, the average crystallite size (d) of HRS was calculated using the Debye–
309 Scherrer model and found to be 43.7 nm. The elemental composition performed by EDX analysis on the
310 fresh (Fig. 1b) and used HRS (Fig. 1c) showed that Fe, O, and Si were the main elements detected in the
311 HRS particles, which is consistent with the results of XRD. More specifically, fresh HRS contained 42.3
312 wt.% O, 40.5 wt.% Fe, and 11.8 wt.% Si. The SEM mapping confirmed the presence of O, Fe, and Si
313 elements in the structure of HRS catalyst.

314 The FESEM and HRTEM results of the sample are shown in Fig. 2. Based on Fig. 2a showing the
315 morphology of fresh catalyst, all the particles were spherical in shape. Comparing the surface
316 morphology of the bare (Fig. 2b) and HRS beads (HRSB, Fig. 2c) indicated that HRSB were rougher and
317 have non-uniform granular bumps, most likely caused by the HRS crosslinking during the integration of
318 them to alginate. The presence of abnormalities on the surface of HRSB could increase the surface area
319 and the number of active sites, which is finally, might improve the catalytic performance (Hu et al., 2019).
320 The HRTEM images of fresh HRS (Fig. 2d) revealed that the sphere-shaped particles were present and

321 homogeneously distributed on the alginate beads. Based on the HRTEM analysis (Fig. 2e), the average
322 size distribution of HRS particles calculated by Digimizer software (5.3.5 version) was 211 ± 52 nm.



323
324 **Fig. 1. (a) XRD pattern, (b) EDX analysis and (c) SEM-mapping of fresh HRS.**



325

326

327

Fig. 2. FESEM images of (a) fresh HRS, (b) bare beads, (c) HRSB; TEM images of (d) fresh HRS, (e) the particle size distribution histogram.

328 In order to determine the oxidation states of the elements that present in the HRS, XPS analysis was
329 done in the range of 0–1200 eV. Fig. 3 shows the XPS analysis results for the fresh and used HRS catalyst.
330 The analysis data in Fig. 3a show that C, O, Fe and Si were present in the HRS catalyst. The C, O and Si
331 spectrums were fitted with Gaussian peaks model based on the literature: more specifically, Fig. 3b gives
332 the XPS spectrum of Si 2p. The peak located at 106.5 eV in fresh HRS indicated that Si existed as Si^{4+} in
333 the Fe-SiO₂ catalysts (Feng et al. 2017). The presence of carbon in XPS spectra is related to the parts of
334 L.O.I that present in the HRS and selection of carbon as reference peak (Naseri and Samadi, 2017). Based
335 on Fig. 3c, 289 eV binding energy is related to C-1s. The O 1s spectrum shows a main peak at 536 eV in
336 Fig. 3d. The fitting Gaussian peak marked at 536 eV is related to the oxygen (i.e., O_2^- ions) that are present
337 in the iron oxide nanomaterials (Rahman and Asiri, 2015). Fig. 3e presents Fe peaks at binding energies
338 at around 716 eV and 730 eV in fresh HRS, which are attributed to the Fe 2p_{3/2} and Fe 2p_{1/2}, respectively
339 that approved the existence of Fe₂O₃ in fresh samples. Due to the strong interaction between iron and
340 silica in our HRS samples, the binding energies for Fe 2p were higher than previously reported data (Yu
341 et al., 2018).

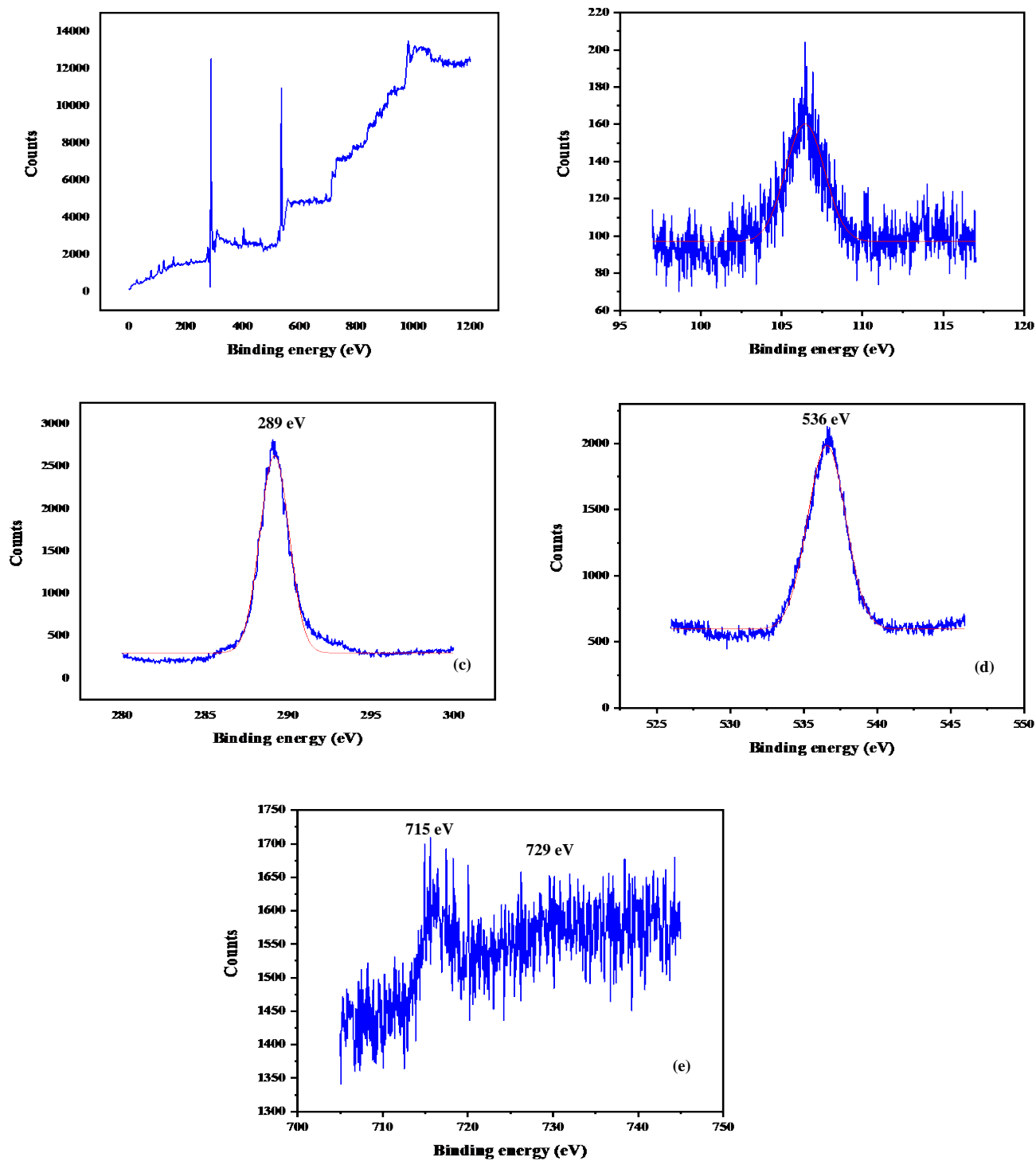


Fig. 3: XPS spectra for (a) fresh HRS, (b) Si 2p, (c) C 1s, (d) O 1s and (e) Fe 2p.

342

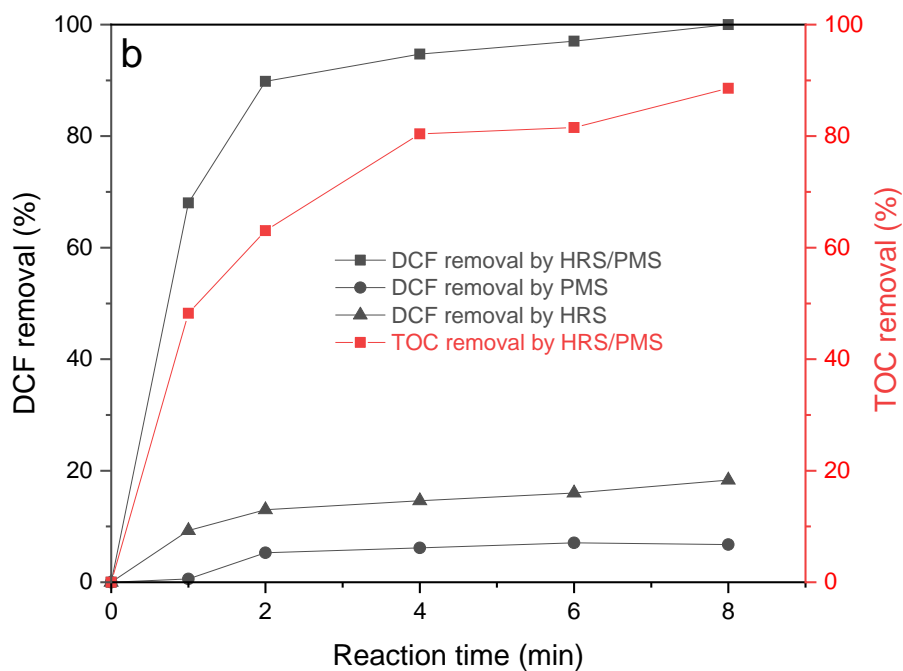
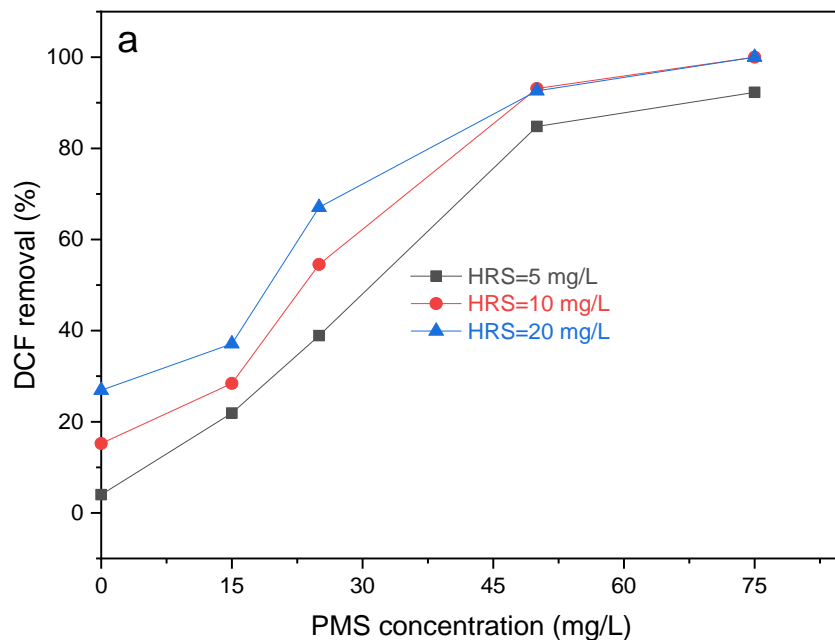
343

344 **3.2. DCF removal by the HRS/PMS process: reaction parametrization**

345 **3.2.1. *Effect of oxidant/catalyst concentration***

346 The removal of Diclofenac (DCF) from an aqueous solution using 5, 10 and 20 mg/L HRS in the presence
347 of various concentrations of PMS between 0 and 75 mg/L was investigated and the results are shown in
348 Fig. 4. We report that 5, 10 and 20 mg/L of HRS could remove (by adsorption) only 5.1, 15.2 and 26.9%
349 of DCF in the absence of PMS within 10 min. Adding PMS to each of the selected HRS concentrations
350 caused significantly improving the DCF removal. For 5 mg/L HRS, the DCF increased from 21.9 to 92.8%
351 when the PMS added to the suspension was increased from 15 to 75 mg/L. The same trend without a
352 significantly higher increase when increasing HRS concentrations from 10 to 20 mg/L; under these
353 conditions the complete removal of DCF was determined at the PMS concentrations of 75 mg/L.
354 Accordingly, 10 mg/L was chosen as the optimal concentration for HRS to efficiently activate PMS and
355 achieve complete removal of DCF in the HRS/PMS process.

356 In order to better illustrate the synergistic effect of adding PMS to the HRS suspension, the DCF removal
357 was recorded as a function of the reaction time in the HRS/PMS process and single HRS and PMS as
358 control conditions, with 10 mg/L HRS and 75 mg/L PMS as the optimal values; the results are given in
359 Fig. 4a. It is observed that in the HRS/PMS process 75.1% of DCF was removed in the first 2 min and
360 extending the contact time to 10 min resulted in its complete removal. In comparison, only 6.8% and
361 18.3% of DCF were removed by single PMS and HRS, respectively, within 10 min. Therefore, the
362 performance of the HRS/PMS process in the DCF removal was much greater than that of single PMS and
363 HRS, and HRS can be considered an effective PMS activator. Indeed, a high degree of synergy ($S > 3$),
364 calculated from Eq. (4), was achieved by combining HRS and PMS for the removal of DCF under the
365 selected conditions.



366

367

368

369

370

Fig.4: a) The effect of HRS on activation of PMS for degradation of DCF (DCF= 50 mg/L; solution pH= 6.5; reaction time= 10 min). b) DCF degradation and mineralization in the HRS/PMS process as a function of the reaction time (DCF=50 mg/L; pH= 6.5; HRS=20 mg/L; PMS (when added)=75 mg/L)

371 The degree of TOC reduction in the HRS/PMS process with 20 mg/L of HRS and 100 mg/L of PMS as a
 372 function of the reaction time is shown in Fig. 4b. Around 48% of TOC was removed in the first 2 min
 373 reaction time and it increased up to 88.5% when the reaction time was prolonged to 10 min. Considering
 374 the results shown in Fig. 4b, the k_{obs} of DCF and TOC reduction in the HRS/PMS under the selected
 375 conditions was determined from Eq. (3) to be 0.334 and 0.208 min^{-1} , respectively. Therefore, a high
 376 degree of DCF degradation and mineralization rate was achieved in the HRS/PMS process under mild
 377 experimental conditions (low natural-catalyst and oxidant concentrations). We report that 50 mg/L DCF
 378 could be completely degraded in the HRS/PMS process with 10 mg/L HRS as the activating catalyst and
 379 75 mg/L PMS. Contextualizing our results with similar literature studies, Table 3 compares the
 380 degradation and mineralization of DCF in our developed HRS/PMS process with previously reported
 381 catalytic AOPs. It is observed that the HRS/PMS process achieved much greater percentages and rates in
 382 the degradation and mineralization of DCF. It implies that the HRS as a natural material catalyst much
 383 more efficient than the previously reported synthesized catalysts for activating PMS.

384

385

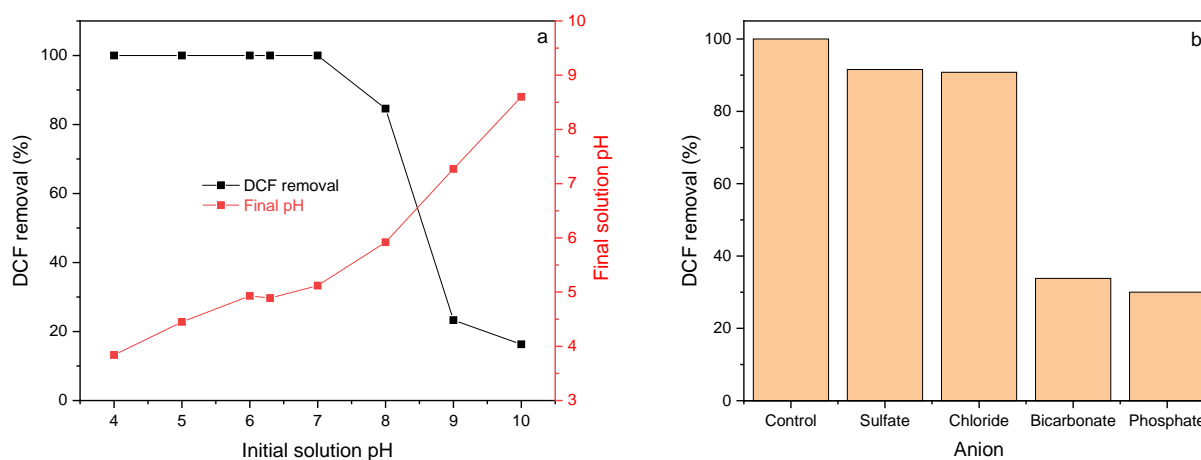
Table 3: DCF removal in different catalytic AOPs.

Catalyst/oxidant	pH	Concentration (mg/L)			Degradation			Mineralization		Reference
		DCF	Catalyst	PMS	RE (%)	k_{obs} (min^{-1})	r_{obs} (mg/L.min)	RE (%)	k_{obs} (min^{-1})	
LaFeO ₃ /PMS	7	3.7	76	600	100	0.016	0.06	----	----	Rao et al., 2019
Co ²⁺ /PMS	3.5	14.8	14.7	38	71	>0.01	>0.01	----	----	Ahmed et al., 2012
CNOMS-2/PMS	5	10	100	200	98.3	0.187	1.87	55	----	Wu et al., 2019
(Co + Ce)-OMS-2/PMS	5	10	180	237	88.4	0.530	5.30	----	----	Wu et al., 2018
Co ₃ O ₄ -g-C ₃ N ₄ /PMS	6.7	10	500	15	100	0.084	0.84	----	----	Shao et al., 2017

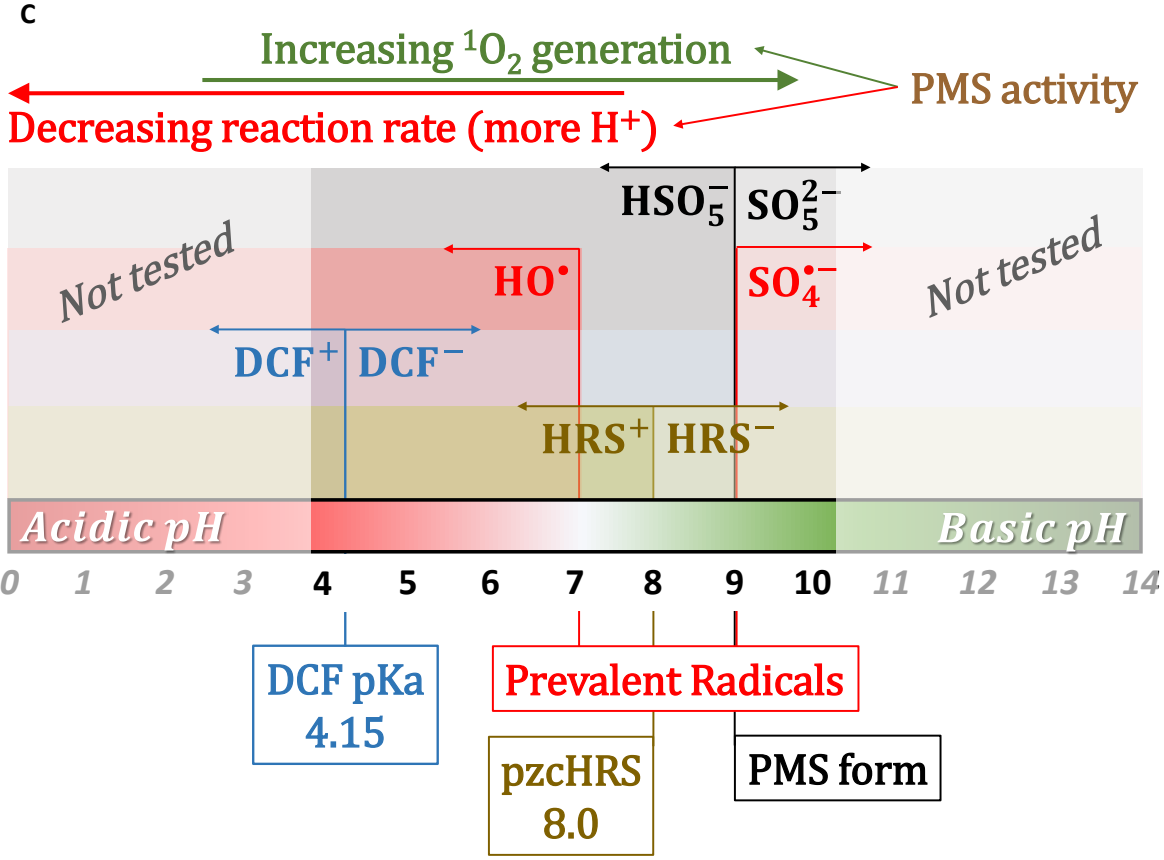
386

387 **3.2.2. Effect of solution pH**

388 The effect of solution pH on the removal of DCF in the HRS/PMS system after 10 min was evaluated
389 between 4 and 10. Fig. 5 indicates that the DCF removal in the developed process is independent of the
390 solution pH up to the neutral conditions ($\text{pH} \leq 7$), where complete removal of DCF was achieved. This
391 suggests that the HRS/PMS process can be efficiently applied for treating contaminated natural waters
392 without needing to adjust the pH to acidic values. The DCF removal was, however, dropped to 84.6, 23.3
393 and 16.3% at the solution pH of 8, 9 and 10, respectively. A similar decrease in DCF removal with the
394 increase in solution pH was also reported for the PMS activated with BiFeO_3 (Han et al., 2020), Co_3O_4 -g-
395 C_3N_4 (Shao et al., 2017) and cobalt-manganese complex (Wu et al., 2019). In comparison, the highest
396 DCF removal was observed in the LaFeO_3 /PMS process at pH 7.0 and it decreased under acidic and
397 alkaline conditions (Rao et al., 2019). Therefore, the influence of solution pH on the performance of a
398 catalyst-activated PMS process is greatly depends on the catalyst properties in the interaction with the
399 solution pH.



400



401

402

403

404

405

406

407

408

409

410

411

Fig. 5a: Effect of initial solution pH on the DCF removal in the HRS/PMS process (DCF=50 mg/L; HRS=10 mg/L; PMS=75 mg/L; contact time=10 min). Fig. 5b: Effect of water anions on the performance of the HRS/PMS process in DCF removal (DCF=50 mg/L; pH=6.5; anions= 100 mg/L). 5c) Analysis of one of the main driving forces of DCF degradation, governed by pH in the PMS/HRS process.

Another factor to take into account should be the pKa of DCF; with a pKa of 4.15, at pH>4.15, the anionic form of DCF⁻ will prevail. However, in terms of the degradation mechanism, PMS could firstly be activated by HRS through the adsorption of PMS onto the surface of the catalyst, followed by the charge transfer between PMS and the catalyst (Othman et al., 2020). Accordingly, the effect of solution pH on the activation of PMS by the HRS catalyst can be explained considering the pKa of PMS and the pH_{pzc} of

412 the catalyst (ca. 8.0) which affected the first step of the activation process. HSO_5^- is the dominant form
413 of PMS species at the acidic to mild-alkaline pHs ≤ 9.4 (Wu et al., 2019; Rao et al., 2019).
414 On the other hand, the HRS has a pH_{pzc} of 8.0 meaning that its surface is positively and negatively
415 charged at the solution pH below and above of 8.0, respectively (Alahabadi and Moussavi, 2017).
416 Therefore, at the acidic to neutral solution pH, the surface of the catalyst had a positive charge,
417 electrostatically attracting HSO_5^- which resulted in its activation and the formation of oxidative species.
418 However, at the alkaline pH the negatively charged catalyst repulsed the PMS anions (HSO_5^- and SO_5^{2-})
419 thus limited the activation process in an increasing manner, and thereby the DCF removal (Wu et al.,
420 2019; Rao et al., 2019). In a nutshell, there are many opposing forces and areas of overlap whose effects
421 seem to peak around 6-7 pH.

422

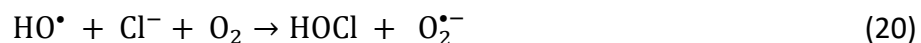
423 **3.2.3. Effect of water anions on DCF degradation performance by HRS/PMS**

424 Natural waters and wastewaters contain different anions which may affect the performance of an AOP,
425 due to the fact that they can react with HO^\bullet and $\text{SO}_4^{\bullet-}$ to form radicals with lower oxidative potential
426 and thus resulting in decreasing the degradation of the target contaminants (Luo et al., 2019). The effect
427 of main water anions on the performance of the HRS/PMS is illustrated in Fig. 5b. We report that the
428 DCF removal decreased from 100% in the absence of anions down to 30% in the presence of 100 mg/L
429 phosphate and 34% in the presence of 100 mg/L bicarbonate, indicating the strong inhibition of the
430 process in the presence of these anions. Phosphate ions can bind with the active sites on the surface of
431 the catalyst thus inhibiting the interaction between PMS and the catalyst and decrease the activation
432 efficacy (Rao et al., 2019). This fact indirectly suggests that the activation of PMS occurred on the surface
433 of the HRS particles. Similar result was observed for DCF degradation in the LaFeO_3 -catalysed PMS

434 process (Rao et al., 2019). On the other hand, the reduction in the DCF degradation in the presence of
435 bicarbonate can be attributed to the point that $\text{CO}_3^{\bullet-}$ with lower oxidation potential might be generated
436 from the reaction between bicarbonate and the reactive species formed in the process (Rommozzi et al.,
437 2020; Zhou et al., 2020).



438 Where the speciation between HCO_3^- and CO_3^{2-} depends on the solution pH. Chloride and sulfate (Fig.
439 5b) did not considerably affected the DCF removal in the HRS/PMS process. Although sulfate at near-
440 neutral pH is unable to scavenge hydroxyl radicals, chloride ions are efficient scavengers, giving rise to
441 Cl^\bullet radicals, as follows (Rommozzi et al., 2020):



442 It is for a fact that these anions are not be able to significantly scavenge the singlet oxygen (Li et al.,
443 2020). Hence, by the negligible effect in our results, we get indirect proof that the process is taking place
444 on the surface of the catalyst and involves a non-radical pathway with $^1\text{O}_2$ generation. Considering that
445 chloride and sulfate are the two of the most abundantly found anions in natural waters, the unaffected
446 performance of the HRS/PMS even dominated by these anions, the generation of $^1\text{O}_2$ suggests that the
447 process could be effectively used for treating contaminated natural waters without inhibitory side-
448 effects of these anions (Wang et al., 2019). **OJO CON ESTE PARRAFO EN AZUL QUE OLVIDA AL RADICAL**
449 **ANION SULFATO, YO LO REORIENTARIA UN POCO PERO TE LO DEJO A TI**

450

451 **3.3. The performance of alginate beads-supported HRS (HRSB) in activating PMS and its reusability:**

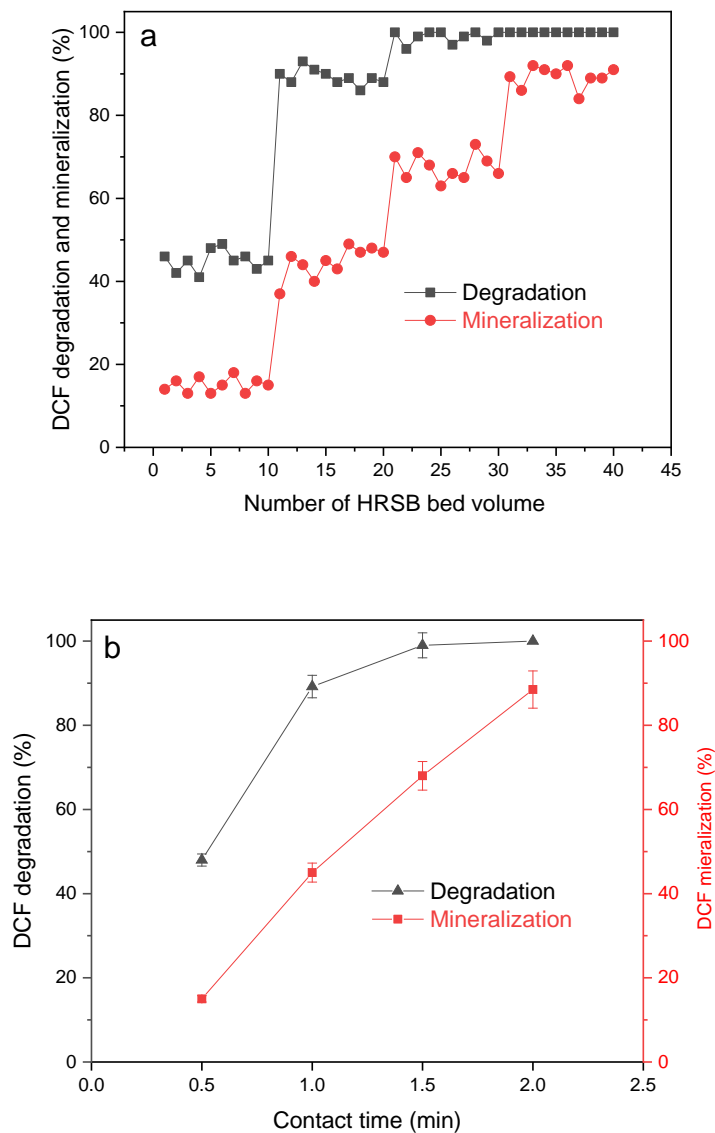
452 **batch and column tests**

453 The HRS/PMS process was firstly run in a heterogeneous activation mode, by HRS supported in alginate
454 beads, in batch. Using 5 granules of HRSB in 50 mL of 50 mg/L DCF solution, supplemented with 75 mg/L
455 PMS, complete degradation of DCF was determined in the HRSB/PMS within 2 min under the selected
456 conditions. At the end of the reaction, the solution was withdrawn from the reactor, the beads were
457 washed twice with distilled water and the test was run again for 5 consecutive times reusing the beads.
458 The results indicated that complete degradation of DCF was achieved for all the reused tests and
459 indicates the beads were efficiently reusable (Fig 6a). It is worth noting that the total concentration of
460 Fe leached from the beads into the solution at the end of the reaction was measured to be 0.03 mg/L,
461 indicating that the catalyst is stable enough for reuse.

462 In order to evaluate the field applicability of the developed process, the second mode of operation took
463 place in a packed bed column; testing of the HRSB/PMS under continuous flow with different HRT was
464 conducted. The degradation and mineralization of 50 mg/L DCF in the flow through packed bed reactor
465 by the HRSB/PMS process as a function of HRT is shown in Fig. 6. We report that complete degradation
466 and 89.3% mineralization of DCF could be achieved at an HRT as low as 2 min. Decreasing the HRT caused
467 a reduction in the performance, particularly in the mineralization efficiency, due to the decrease in the
468 contact time between PMS and the catalyst; the catalytic system was apparently unable to generate
469 sufficient amount of oxidizing species degrading the DCF degradation byproducts alongside the DCF. The
470 aforementioned high stability along with the efficient removal of DCF in a flow through packed bed
471 reactor by the HRSB/PMS process of the present study, clearly confirms that the HRSB is a very promising

472 and sustainable natural catalyst for activating PMS to be used for the efficient and cost-effective
 473 degradation of emerging contaminants.

474



475

476 **Fig. 6: (a) Stability of the HRSB in repetitive cycles of DCF degradation, (b) DCF degradation and mineralization**

477 **in the packed bed HRSB/PMS process as a function of HRT (DCF=50 mg/L; PMS=75 mg/L; pH=6.5).**

478

479 **3.4. Simultaneous disinfection and decontamination: *Escherichia coli* and *Enterococcus sp.***

480 ***inactivation by the batch HRS/PMS process in presence/absence of DCF***

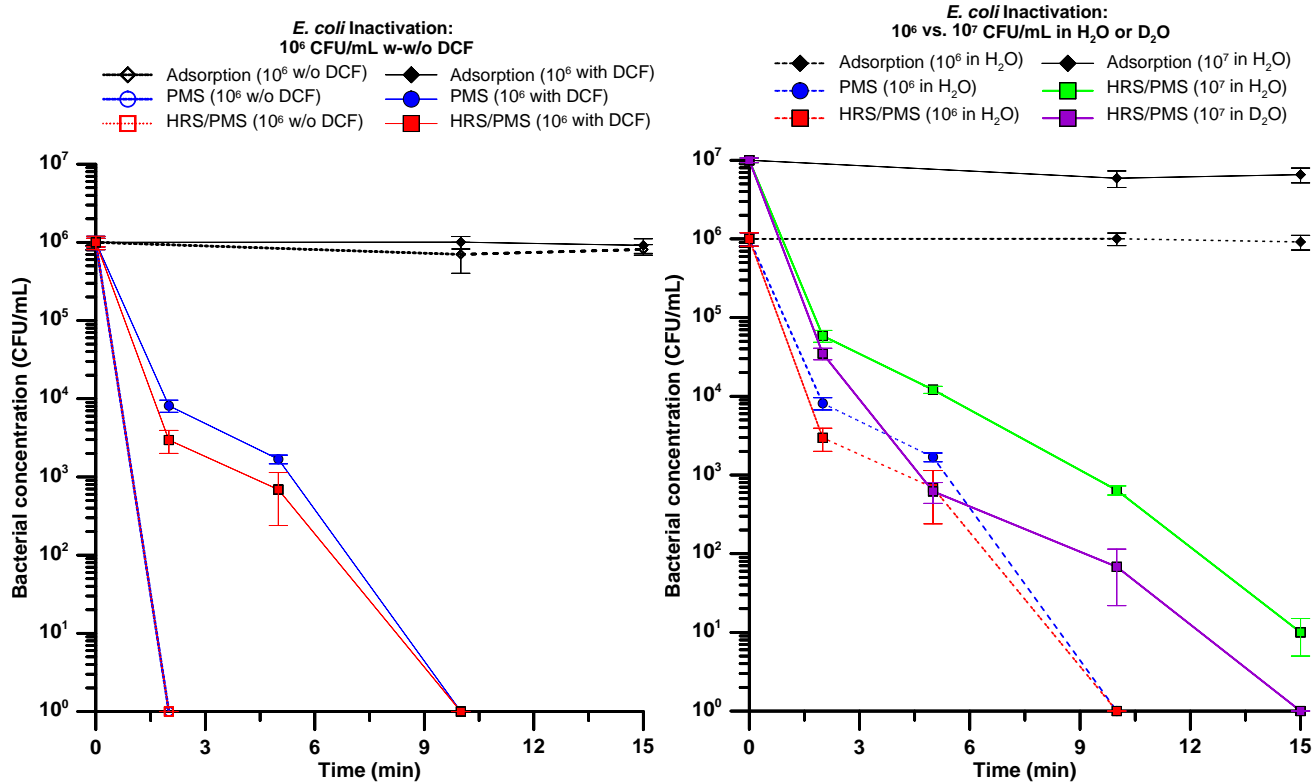
481 In order to assess the disinfection capacity of the HRS soil as a PMS activator, *E. coli* and *Enterococcus*
482 *sp.* inactivation tests were performed, as representative bacteria of the Gram-negative and Gram-
483 positive categories, and the results are summarized in Fig. 7. Since the HRS/PMS process was found to
484 be very synergic, the different actions taking place were attempted to be dissociated, in the elimination
485 of the new, microbial targets. The first set of experiments took place in absence of DCF, in distilled water
486 (Fig. 7a). The addition of 10 mg/L HRS did not affect cultivability, and the adsorption of HRS to *E. coli* cells
487 did not reduce the viable count. HRS at pH = 6.5 is positively charged and bacteria carry a negative
488 charge. However, HRS has a mean diameter of 211 nm, while bacteria are μm sized microorganisms.
489 Hence, the HRS adsorption did not cause aggregates that affected the bacterial concentration.

490 The addition of 75 mg/L PMS caused rapid inactivation (within 2 min), which indicated the sensitivity of
491 this target against PMS. PMS could abstract electrons from cell wall components (e.g. carboxylic acids),
492 oxidize them and generate $\text{SO}_5^{\bullet-}$ radicals, which inactivate bacteria by themselves, or be a precursor of
493 $^1\text{O}_2$ generation (Eqs. 4,5). Naturally, with the addition of HRS for PMS activation bacteria were also
494 inactivated in less than 2 min, with the induction of radicals' generation, albeit too fast to be measured.
495 Following, addition of DCF in the bacterial dispersion was assayed. Although the presence of DCF did not
496 affect *E. coli* adsorption, it presented an antagonism for the direct oxidation by PMS; DCF competes with
497 *E. coli*, hence a delay was presented, and bacteria were inactivated within 10 min. Notably, the addition
498 of HRS led to a modest increase in *E. coli* inactivation kinetics. This effect indicates that either 10 mg/L
499 HRS does not enhance the generation of bactericidal species (not enough catalyst), or that the ones
500 generated by PMS are already germicidal enough. Most likely, it could be a kinetic limitation driven by
501 the adsorption of HRS onto bacteria.

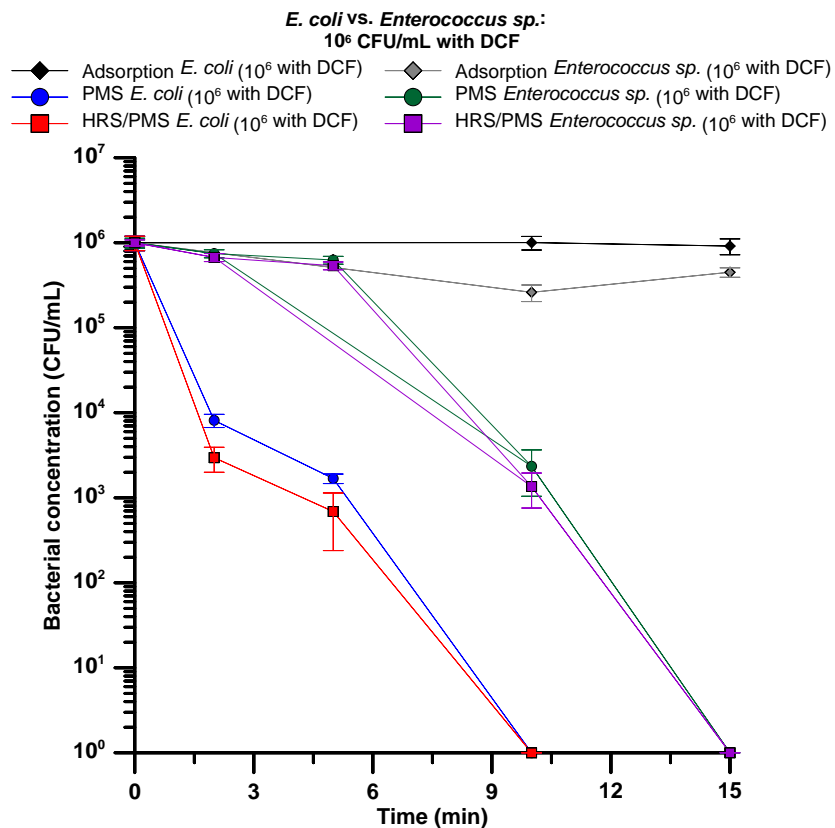
502 In order to further investigate the germicidal species generated by the HRS/PMS process, we increased
503 the bacterial concentration 10-fold, still in presence of DCF, and the results are given in figure 7b. A small
504 increase in residence time (15 min) led to a 6-log bacterial inactivation. The kinetics still fit a log-linear
505 inactivation profile, but the concentration increase hindered the inactivation process (reactant
506 limitations and target competitions possible). Another assay that has been carried out was by
507 introducing 50% D₂O in the water, in order to study the kinetic isotope effect and probe a possible singlet
508 oxygen participation. Singlet oxygen is “scavenged” multiple times faster in water compared to its
509 deuterated isotope, hence a possible enhancement in inactivation may indicate the participation of ¹O₂.
510 Interestingly, the inactivation rate increased, and total bacterial elimination was achieved in 15 min. In
511 previous studies, the inactivation rates induced by HO•, SO₄•⁻ and ¹O₂ have been measured to 2.5x10¹¹,
512 ~1x10¹¹, and 2.4-3.8x10⁷ M⁻¹ s⁻¹ respectively (Kohantorabi et al., 2019; Serna-Galvis et al., 2018-147).
513 Although this rate seems small, when compared with other organic compounds it is not a negligible
514 effect (e.g. 10⁵-10⁶ M⁻¹ s⁻¹ for phenols) (Scully Jr. and Hoigné, 1987). Hence, if there is singlet oxygen
515 participation in bacterial inactivation, its participation in DCF degradation should also be considered. **NO**
516 **LO ENTIENDO BIEN**

517 Finally, in order to broaden the applicability of the findings, besides *E. coli* (Gram-negative), the
518 inactivation of *Enterococcus sp.* as a model Gram-positive strain was also assessed, in presence of DCF.
519 The control tests (adsorption) showed practically no difference between the two strains. However, the
520 inactivation by the PMS and PMS/HRS processes, was again similar between the two strains, but
521 presenting completely different kinetics. *E. coli* were inactivated following immediate decay upon
522 treatment, while *Enterococcus sp.* showed a lag period before their inactivation started. Lag-phases are
523 associated with the need to accumulate damages before reaching the inactivation. The HRS/PMS system

524 is a process that generates oxidative species in the bulk, and these reactive species attack the cell walls
 525 of microorganisms, leading to their inactivation (interested readers in the mechanism of inactivation
 526 should refer to (Xiao et al., 2019, 2020). The Gram-positive bacteria have significantly different structure
 527 than Gram-negative. Since the process generates a specific amount and type of oxidants, then the
 528 difference lies in the composition of the cell wall, with Gram-negative consisting of polysaccharides and
 529 a mono-layer of peptidoglycan, while Gram-positive have multiple layers of peptidoglycan before the
 530 cell membrane, respectively. Hence, the different structure and the different reactivity of radicals with
 531 the components (10^7 - $10^{10} \text{ M}^{-1} \text{ s}^{-1}$) can result to the big variation observed. Nevertheless, as a provisional
 532 conclusion, we can highlight that 10^6 CFU/mL bacteria are eliminated much before DCF (as independent
 533 targets) while their simultaneous presence does not significantly hinder the efficacy of the system.
 534



535



536

537 **Figure 7 - Bacterial inactivation in the HRS/PMS system at near-neutral pH (6.5). A) *E. coli* inactivation (10⁶**
 538 **CFU/mL) in presence/absence of 50 mg/L DCF by PMS 75 mg/L, PMS/HRS : 75/10 mg/L (adsorption as blank).**
 539 **B) 10⁶ or 10⁷ CFU/mL *E. coli* inactivation by PMS, PMS/HRS (adsorption for blank) in water. The purple is in D₂O**
 540 **which shows the important ¹O₂ pathway. C) *E. coli* vs. *Enterococcus* sp. (gram-Negative vs. gram-Positive**
 541 **bacteria) at 10⁶ CFU/mL.**

542

543 **3.5. DCF degradation mechanism in the HRS/PMS process: action modes, radical vs. non-radical**
 544 **degradation mechanisms and transformation pathways**

545 From the results so far, we can verify that the notable activity of HRS for the removal of DCF and
 546 microorganisms in water is the net sum of a number of processes. In this part, in order to fully elucidate
 547 the full path towards elimination, we focus on the four distinct steps: analysis of the (theoretically)

548 involved processes, examination of the physicochemical properties of the catalyst, scavenging tests and
549 radical determination, and finally, DCF degradation pathway.

550

551 **3.5.1. Dissociating the complex catalytic process**

552 First, we attempt to dissociate the occurring processes in order to further elucidate the mechanism of
553 DCF removal and bacterial inactivation. The occurring actions can be separated to:

554 **1. Adsorption.** Adsorption of the contaminant (biological or chemical) onto HRS would be the first step
555 of the complex degradation process since PMS and HRS need to come in contact, in order to achieve
556 activation and generate the reactive species responsible for disinfection/decontamination. HRS at pH
557 6.5 presents a positive charge which in conjunction with the negative charge of DCF ($pK_a = 4.15$) or the
558 overall negative charge of bacteria (due to their teichoic acids and peptidoglycans), present an
559 electrostatic attraction that enhance the adsorption to HRS. We have measured a ~15% of DCF removal
560 only by HRS, that could be attributed to the adsorbed DCF, but insignificant bacterial reduction.

561 **2. Direct, PMS-driven oxidation, without activation.** PMS is a stable oxidant with a 1.81 V oxidation
562 potential, that can directly react with organic contaminants, including DCF (Yang et al., 2018), as well as
563 bacteria, as seen in our results and other studies (Rodríguez-Chueca et al., 2019). Its effects are
564 noticeable even without activation in high concentrations that overcome the kinetic limitation. In the
565 present study, we have measured a ~10% DCF reduction due to direct PMS oxidation and a 6-logU
566 bacterial reduction, at 75 mg/L. Hence, the direct PMS action has to be accounted for, via its $SO_5^{\bullet-}/^1O_2$
567 generation, reaction with DCF and the direct oxidation of membrane components (cell wall potential
568 ~0.7 V), also possibly via the aforementioned routes.

569 **3. PMS Activation by HRS:** The generation of oxidative species passes through the activation of PMS and
570 then results to the oxidation of the targets. Depending on the reaction localization, the activation could
571 be either:

572 *i) Homogeneous PMS activation (leached Fe-HRS/PMS system):* We have measured a small but
573 existent amount of dissolved Fe in the bulk of the medium after reaction (at pH=7). Because
574 of the iron leaching measured, an effective Fe-mediated catalytic cycle takes place, which
575 results in the generation of HO^* , $\text{SO}_4^{\bullet-}$ and $\text{SO}_5^{\bullet-}$ radicals. As a result, although at more acidic
576 conditions this contribution is expected to be higher, we suggest its importance at the studied
577 conditions, i.e. that this pathway of activation is actively contributing to disinfection and
578 decontamination.

579 *ii) Heterogeneous PMS activation (interfacial HRS/PMS action):* The reactions that take place in
580 the interface between HRS and PMS are expected to further contribute in DCF degradation
581 and bacterial inactivation. These reactions are governed by the pH, causing the electrostatic
582 repulsion/attraction between catalyst and PMS or target (bacteria/DCF), and the type of
583 radical that is generated. Generally, activation of PMS and generation of oxidative species take
584 place with the Fe bound on the surface of the HRS catalyst and cycling must take place there,
585 hence different k rate constants need to be considered. Nevertheless, this pathway is not
586 straightforward and in order to define the degradation pathway, we would need to check the
587 oxidation state of the catalyst and the reactive species generated from the HRS/PMS process.

588

589 **3.5.2. Structural, chemical, and morphological changes of the HRS catalyst**

590 In order to begin the elucidation of the degradation processes, first we assessed the changes in the
591 catalyst. After experimentation in the HRS/PMS system, the catalyst was recovered, and its
592 characterization was performed anew; the results are summarized in Figure 8. The HRTEM after the
593 catalytic reaction showed that the HRSB maintained a similar shape with the same size as the pristine
594 HRSB, confirming the good structural stability of the prepared beads. Hence, the comparison of the rest
595 of its properties is valid since the catalyst was not significantly altered.

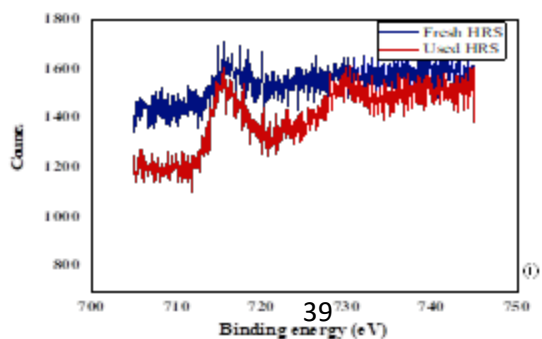
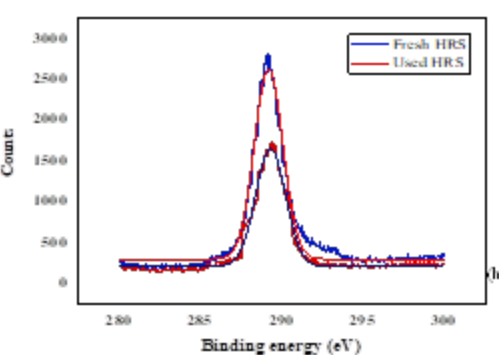
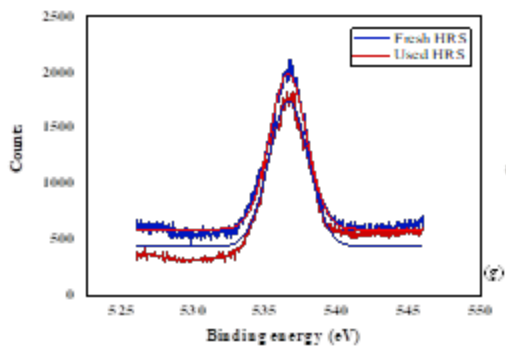
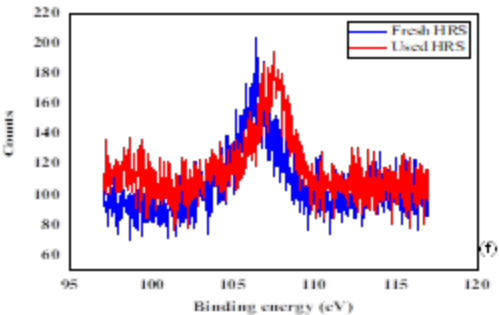
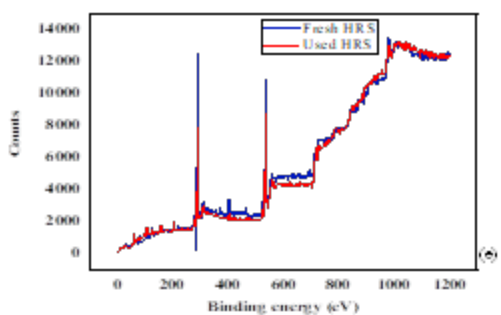
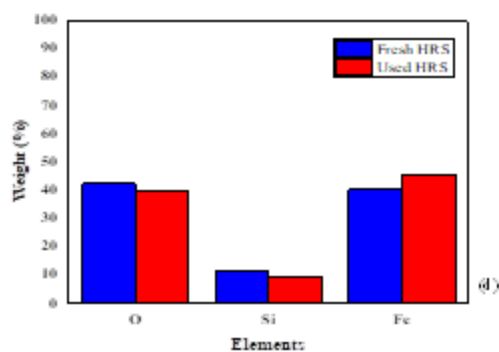
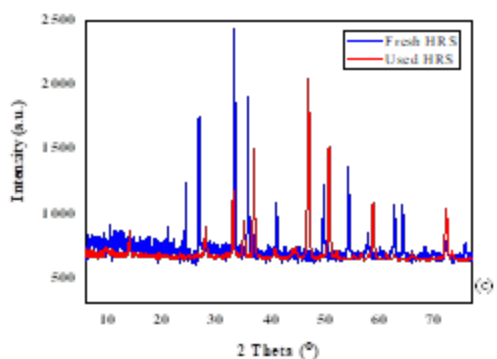
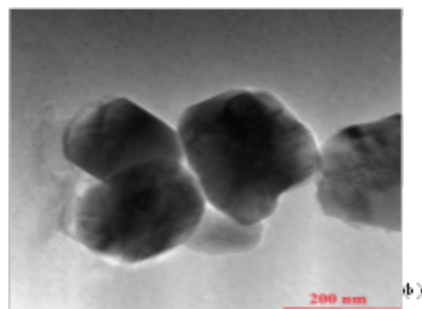
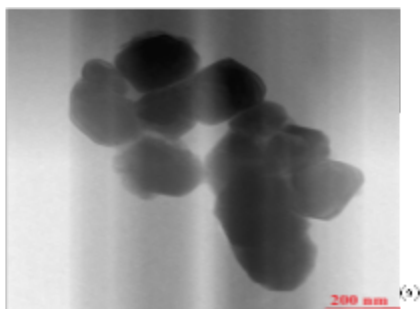
596 The XRD patterns revealed that the principal constituents of the HRS were α -Fe₂O₃ and SiO₂. A part of
597 Fe₂O₃ in the catalyst, after being used in the degradation of DCF, was reduced to Fe₃O₄, which could be
598 verified by the diffraction peaks at 30.035°, 35.442°, 43.065°, 53.373°, 56.873°, 62.552° in the XRD
599 pattern (Fig. 8) (Deng and Li, 2018), instead of 28.1, 38.7, 41.6, 47.83, 58.1, 63.7, 67.9, 74 and 75.9° of
600 the pristine HRS catalyst.

601 Furthermore, the fresh HRS contained 42.3 wt.% O, 40.5 wt.% Fe, and 11.8 wt.% Si. After using the
602 catalyst for the activation of PMS, the wt.% of O, Fe and Si were 31.6, 59.6, and 5.7, respectively. This
603 change in elemental composition is related to the minor formation of Fe₃O₄ in the reduced hematite
604 after the reaction (Wei et al., 2019) with PMS, proved by the XRD patterns of fresh and used HRS.

605 The peak located at 106.5 eV in fresh HRS that has shifted to 107.4 eV in the used sample indicates that
606 Si existed as Si⁴⁺ in the Fe-SiO₂ catalyst (Feng et al., 2017). The Fe peaks at binding energies at around
607 716 eV and 730 eV seen in the fresh HRS were attributed to the Fe 2p_{3/2} and Fe 2p_{1/2}, respectively, from
608 the hematite Fe₂O₃ in the fresh samples. In the used sample the peaks at binding energies in the range
609 of 715 eV and 729 eV are related to the Fe 2p_{3/2} and Fe 2p_{1/2} of Fe₃O₄ for used HRS. Feng et al. (2017)
610 reported that the shakeup satellite peak at 719.0 eV (Fe 2p_{3/2}) was fingerprint of the electronic structure
611 of Fe³⁺.

612 Hence we have the first indication of the PMS activation mechanism, where electron abstraction from
613 PMS to reduce Fe^{3+} to Fe^{2+} took place with simultaneous $\text{SO}_5^{\bullet-}$ generation, as a first step, and the Fe^{2+}
614 activation of PMS as a second step, that generates Fe^{3+} and $\text{SO}_4^{\bullet-}$. The measured change in the
615 percentage of Fe may also indicate a small loss in the bulk. Also, the shift in the peak of the XPS spectrum
616 verifies the formation of magnetite and validate the proposed cycle.

617



619 **Figure 8 – Fresh vs. used HRS catalysts changes. A) TEM of the pristine catalyst B) TEM of the used catalyst. C)**
620 **XRD analysis of the fresh (blue) and used catalyst (red). D) EDX analysis of the fresh (blue) and used catalyst**
621 **(red). XPS analysis for the fresh (blue) and used catalyst (red): E) HRS, F) Si 2p, G) C 1s, H) O 1s and I) Fe 2p.**
622

623 **3.5.3. Identifying the degradation mechanism: Radical scavenger testing and EPR measurements**

624 Following, by employing EPR spectroscopy and the choice of proper scavenging tests, we will attempt to
625 resolve the composite action found in the HRS/PMS system and unveil the pathways towards DCF
626 degradation. Most likely, the same pathways will be true for bacterial inactivation, but the outcome of
627 their inactivation is also subject to their reactivity with the generated transient species (Kohantorabi et
628 al., 2019; Serna-Galvis et al., 2018, 2019).

629 The degradation of DCF in the heterogeneous activation of PMS might occur through radical ($\text{HO}^\bullet/\text{SO}_4^{\bullet-}$)
630 mechanism, according to Eqs. 1-3, or the singlet oxygenation and mediated electron transfer non-radical
631 mechanism of Eqs. 4-5 (Othman et al., 2020). Furthermore, the secondary reactions 6-11 cannot be
632 disregarded, hence the identification of the radical species ($\text{HO}^\bullet/\text{SO}_4^{\bullet-}/^1\text{O}_2$) participating in DCF
633 degradation is crucial.

634 EPR experiments employing TEMP (100 mM), a well-known radical spin trap of $^1\text{O}_2$ that results in the
635 formation of a stable TEMPO radical with three-equal intensity pattern signal (REF), were conducted in
636 the presence of PMS (75 mg/L) and HRS (10 mg/L) in aerated media. Control experiments in which only
637 TEMP was employed in the absence or in the presence of PMS or HRS were performed in parallel. All the
638 experiments were carried out in D_2O to enhance the prospects of TEMP to trap $^1\text{O}_2$ since its lifetime is
639 more than one order of magnitude larger than in H_2O (REF).

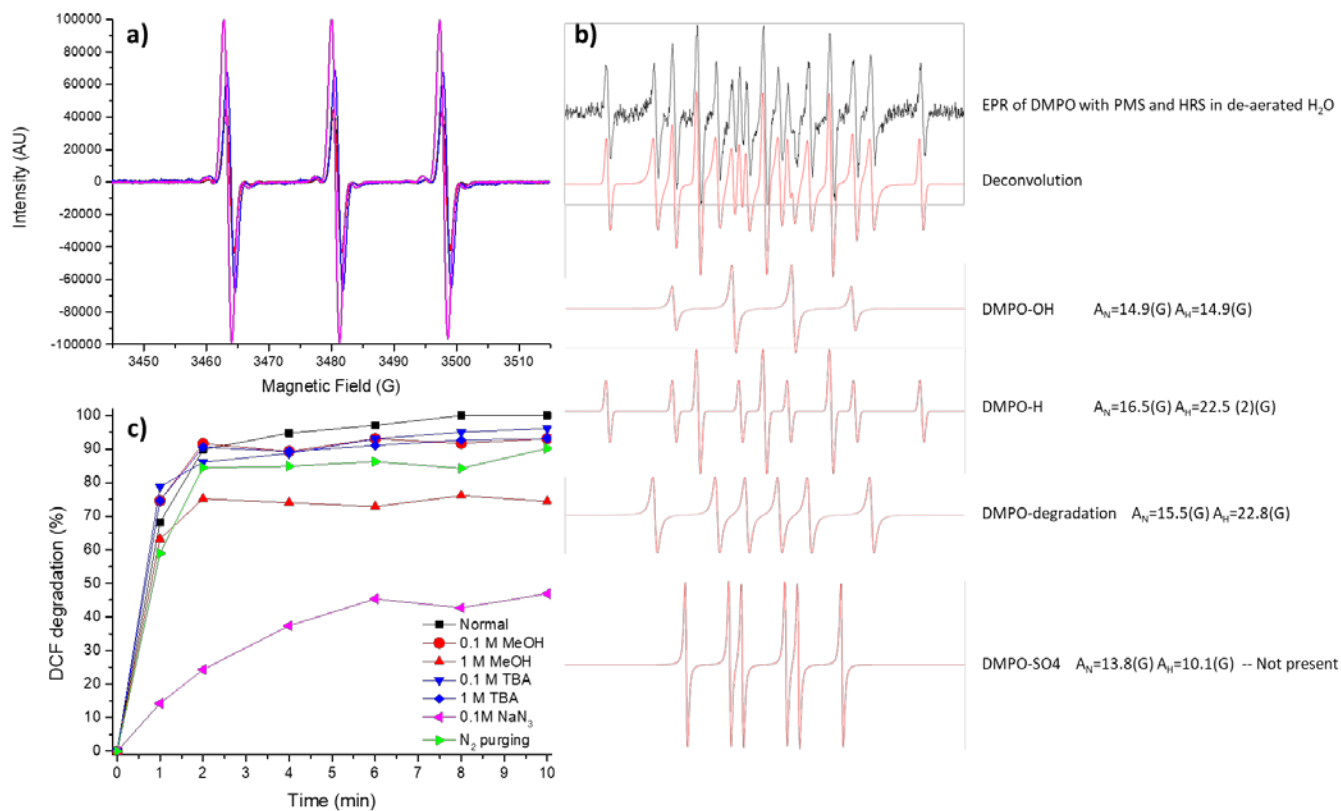
640 Results showed the formation of the typical TEMPO signal (Figure 9a). The highest amount of TEMPO
641 was observed when PMS and HRS were present together in the aerated TEMP mixtures. However, while
642 samples of TEMP alone and with HRS show the similar amounts of TEMPO, its generation increased in
643 mixtures of TEMP and PMS. In the presence of PMS, TEMPO formation is produced by initial TEMP
644 oxidation ($\text{TEMP}^{\cdot+}$), followed by subsequent deprotonation and reaction with O_2 . This process has been
645 described for aerated TEMP mixtures in the presence of oxidants different from PMS (REF). According to
646 the intensity of the TEMPO signal formed from TEMP-PMS mixtures in the absence and in the presence
647 of HRS, more than 30% of the signal intensity can be attributed to the formation of $^1\text{O}_2$.

648 Experiments in the presence of DMPO were performed to confirm the presence of intermediates of
649 radical nature such as HO^{\cdot} and/or $\text{SO}_4^{\cdot-}$ in the aqueous mixture of PMS and HRS. Interestingly, while
650 control experiments in the absence of PMS or HRS did not showed any signal, several spin adducts were
651 detected after a careful deconvolution of the signals obtained from the aqueous DMPO (100 mM) in the
652 presence of PMS (75 mg/L) and HRS (10 mg/L) (see Figure 9b). Thus, DMPO-OH, DMPO-H (which proves
653 the participation of reaction 1) and a mixture of compounds associated to DMPO-degradation were
654 identified, while the one corresponding to DMPO- SO_4 was absent.

655 However, the absence of the DMPO- SO_4 signal does not discard its generation upon reaction of PMS and
656 HRS because the lifetime of the DMPO- SO_4 adduct in H_2O is very short and quickly evolves to the
657 formation of DMPO-OH (REF). In this context, additional experiments were carried out in order to
658 confirm that the DMPO-OH signal could be attributed to the initial formation of HO^{\cdot} and/or $\text{SO}_4^{\cdot-}$,
659 working under the assumption that the absence of DMPO- SO_4 does not preclude its formation since once
660 formed, DMPO- SO_4 quickly evolves to the longer-lived DMPO-OH. In these tests, $\text{SO}_4^{\cdot-}$ was generated by
661 homolytic rupture upon irradiation of a deaerated aqueous solution of $(\text{NH}_4)_2\text{S}_2\text{O}_8$ (75 mg/L) in the

662 presence of DMPO (10 mM) (see details in the Supplementary figures S3-S5). Only when a high
 663 concentration of $\text{SO}_4^{\bullet-}$ was generated by keeping a constant irradiation, a mixture of two different signals
 664 could be observed attributed to DMPO- SO_4 and DMPO-OH. Nevertheless, once the irradiation was
 665 stopped only DMPO-OH could be observed. Hence, the appearance of DMPO-OH as a result of the
 666 reaction between PMS and HRS does not provide an unambiguous piece of evidence for the HO^\bullet
 667 generation.

668 Hence, from the EPR experiments, we can provisionally conclude that the reaction between PMS and
 669 HRS in aerated aqueous media gives rise to the formation of $^1\text{O}_2$, as it was demonstrated when TEMP
 670 was used as spin-trap, while experiments in the presence of DMPO provide evidence for the participation
 671 of HO^\bullet and/or $\text{SO}_4^{\bullet-}$, but do not confer certainty over their participation and importance.



672

673 **Figure 9 – Radical identification tests. A) EPR of aerated D₂O mixtures of TEMP 100 mM, PMS 75 mg/L and HRS**
674 **10 mg/L (pink). Controls: TEMP 100 mM and HRS 10 mg/L (red); TEMP 100 mM and PMS 75 mg/L (blue) and**
675 **TEMP 100 mM (black). B) EPR of DMPO 100 mM, PMS 75 mg/L and HRS 10 mg/L in deaerated H₂O (in black)**
676 **and the deconvolution of the obtained signals (in red). C) Effect of different radical scavengers on the DCF**
677 **removal in the HRS/PMS process (DCF=50 mg/L; pH= 6.5; HRS=10 mg/L; PMS=75 mg/L)**

678

679 Afterwards, a series of selective intermediate quenching tests were implemented in order to determine
680 the predominant reactive species for the DCF degradation in the PMS/HRS system. The quenching agents
681 were MeOH, TBA and NaN₃ (Figure 9c).

682 DCF degradation by PMS and HRS was initially performed in the absence of scavengers, and at the same
683 concentration of the three quenchers (0.1 M). From the comparison of the experimental results,
684 inhibition of the DCF degradation was only observed in the presence of NaN₃. This result can be easily
685 understood because it has been reported that NaN₃ traps HO•, SO₄^{•-} and ¹O₂, while MeOH and TBA only
686 traps HO• and SO₄^{•-}. Besides, NaN₃ shows higher reaction rate constants ($k_{\text{OH}^\bullet} = 2.5 \times 10^9 \text{ M}^{-1} \text{ s}^{-1}$, $k_{\text{SO}_4^{\bullet-}} =$
687 $1.2 \times 10^{10} \text{ M}^{-1} \text{ s}^{-1}$ and $k^1_{\text{O}_2} = 1.0 \times 10^9 \text{ M}^{-1} \text{ s}^{-1}$) than those described for MeOH ($k_{\text{OH}^\bullet} = 9.7 \times 10^8 \text{ M}^{-1} \text{ s}^{-1}$ and
688 $k_{\text{SO}_4^{\bullet-}} = 3.2 \times 10^6 \text{ M}^{-1} \text{ s}^{-1}$) and for TBA ($k_{\text{OH}^\bullet} = 6.0 \times 10^8 \text{ M}^{-1} \text{ s}^{-1}$ and $k_{\text{SO}_4^{\bullet-}} = 4.0 \times 10^5 \text{ M}^{-1} \text{ s}^{-1}$) (REF, (Anipsitakis
689 and Dionysiou, 2004)).

690 Interestingly, a deeper analysis of these results seems to indicate that HO• must not be the main
691 intermediate involved in the DCF degradation, because the k_{OH^\bullet} for the three quenchers has similar
692 values and they were used at the same molar concentration (0.1 M) but degradation of DCF is only
693 diminished by NaN₃. Further support was found using 1 M concentrations of MeOH and TBA in this study,
694 because if the main radical involved in this process was HO•, the presence of MeOH and TBA at 1 M
695 (both have close k_{OH^\bullet}) would generate an effect similar between them and higher than that observed

696 using NaN_3 at 0.1 M. As this was not the case, consequently, the main reactive species should be $\text{SO}_4^{\bullet-}$
697 because the DCF degradation was diminished in the presence of 1 M MeOH but not by 1 M TBA in
698 agreement with a value of the $k_{\text{SO}_4^{\bullet-}}$ by MeOH of ca. one order of magnitude higher than that described
699 for TBA (see values above).

700 Moreover, the role of $\text{SO}_4^{\bullet-}$ as the main intermediate involved the DCF degradation is also in agreement
701 with the high effect observed using NaN_3 at 0.1 M because its $k_{\text{SO}_4^{\bullet-}}$ is more than 1000 times higher than
702 that of MeOH. Nevertheless, a minor effect of $^1\text{O}_2$ in the DCF degradation could not be disregarded
703 because the in the absence of oxygen a lower degradation percentage was observed (see in Figure 9c,
704 results under anaerobic conditions).

705 Hence we can conclude that the combination of the scavenger tests and the EPR experiments clearly
706 confirm that the main intermediate of DCF degradation is $\text{SO}_4^{\bullet-}$ and the participation of $^1\text{O}_2$ in this process
707 is not negligible, while HO^\bullet participation is significantly less important.

708 Finally, having identified the elements that participate in the reaction, its mode (primarily heterogeneous
709 degradation) and the participating radicals, a proposition for DCF degradation would be as follows:

710 - PMS produces $\text{SO}_4^{\bullet-}$ after activation by the HRS soil containing metal oxides such as α -
711 $\text{Fe}_2\text{O}_3/\text{Fe}_3\text{O}_4$ through its adsorption onto the catalyst's surface, followed by the charge transfer
712 contributed by the redox centers and oxygen defects present in the lattice of the α - Fe_2O_3 surface
713 between PMS molecules and the catalyst. (Huang et al., 2013) reported that high catalytic activity
714 of α - Fe_2O_3 was related to the presence of active lattice oxygen in the structure of hematite. The
715 α - Fe_2O_3 in the HRS might also mediate transferring the electrons from DCF molecules to PMS
716 (Tian et al., 2017; Ahn et al., 2016) which could be resulted in PMS reduction (with $\text{SO}_5^{\bullet-}$

717 formation) and thus DCF oxidation. The co-existence of different transition metals of Mn, Ti, Cu,
718 Mg, and Zn as well as Si might also improve the catalytic potential of HRS (Liang et al., 2010).

719 - Another reason for the enhanced catalytic potential of the HRS might be the presence of sulfur
720 (1 wt.%) and calcium (1.3 wt.%) in the structure of the catalyst which could enhance the electron
721 transfer from $\alpha\text{-Fe}_2\text{O}_3$ to PMS thus accelerating acceleration of $\text{SO}_5^{\bullet-}$ radical and singlet oxygen
722 generation (Zheng et al., 2019; Guo et al., 2020). In addition, the presence of the oxygen
723 vacancies/defects in the surface of the catalyst, as a natural material, could decrease the reaction
724 barrier of PMS and thereby improve its activation (Gao et al., 2019; Yang et al., 2020). Therefore,
725 the interaction with $\text{SO}_4^{\bullet-}$ and $^1\text{O}_2$ rather than with HO^\bullet is proposed to be the main mechanism
726 for the degradation of DCF in the developed HRS/PMS process.

727 - Although small, the contribution of singlet oxygen is promising: despite its mild redox potential
728 (0.64-0.81 V) (Diaz-Urbe et al., 2010), it has a long lifetime (up to $\sim 4 \mu\text{s}$ in water, Kohantorabi et
729 al., 2019) and selectivity toward the electron-rich compounds (Chen et al., 2019; Liu et al., 2018),
730 and suggests that the developed process could be an efficient method of treating waters
731 contaminated with compounds bearing electron-rich moieties such as DCF (Nihemaiti et al.,
732 2018).

733

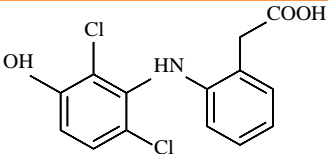
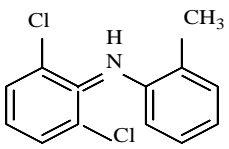
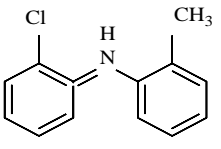
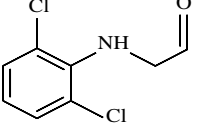
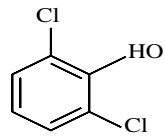
734 **3.5.4. DCF degradation pathway in the HRS/PMS process: LC/MS analysis**

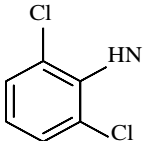
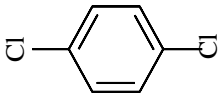
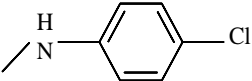
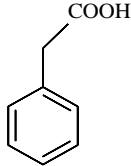
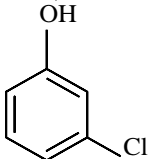
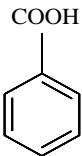
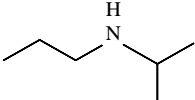
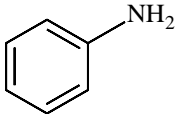
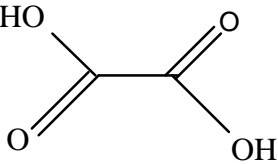

735 The LC-MS analysis was carried out in the positive mode to determine the formation of intermediates
736 during the degradation of DCF in the HRS/PMS process. The transformation products (TPs) were
737 identified when DCF was degraded with 10 m/g HRS and 75 mg/L PMS within the reaction times of 2 and


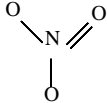
738 10 min. Based on the results of LC-MS analysis in reaction times of 2 and 10 min, 17 actual mass to charge
 739 (m/z) values corresponded to 17 TPs were identified. Based on the identified intermediates given in
 740 Table 4, a pathway was proposed for DCF degradation in the HRS/PMS process as Fig. 10. According to
 741 the LC/MS analysis, the different mechanisms that were deduced to be involved in the degradation of
 742 DCF in the HRS/PMS process, including the hydroxylation, dehydroxylation, dechlorination, C-N bond
 743 cleavage, decarboxylation, and further benzene-ring opening towards the formation of aliphatic
 744 compounds e.g. carboxylic acids (Moradi et al., 2020; Rao et al., 2018).

745

746 **Table 4: The transformation products of DCF degradation in the HRS/PMS process.**

Row	M/Z	Chemical formula	Structure	Adduct	Reaction time (min)
1	312	C ₁₄ H ₁₂ Cl ₂ NO ₃		[M+Na] ⁺	2
2	252	C ₁₃ H ₁₁ Cl ₂ N		[M+K] ⁺	2
3	216	C ₁₃ H ₁₁ ClN		[M+ACN+H] ⁺	2
4	207	C ₈ H ₁₁ Cl ₂ NO		[M+ACN+H] ⁺	10
5	163	C ₆ H ₄ Cl ₂ O		[M+K] ⁺	2

6	161	$C_6H_4Cl_2N$		$[M+H]^+$	2
7	147	$C_6H_4Cl_2$		$[M+H+2Na]^+$	2
8	141.5	C_7H_8ClN		$[M+K]^+$	2
9	136	$C_8H_8O_2$		$[M+K]^+$	2
11	128	C_6H_5ClO		$[M+ACN+H]^+$	10
12	122	$C_7H_6O_2$		$[M+H+Na]^+$	2
13	101.1	$C_6H_{15}N$		$[M+ACN+H]^+$	10
14	93	C_6H_7N		$[M+ACN+H]^+$	10
15	90	$C_2H_2O_4$		$[M+2H]^+$	2
16	89	$C_2H_2O_4$		$[M+3Na]^+$	2

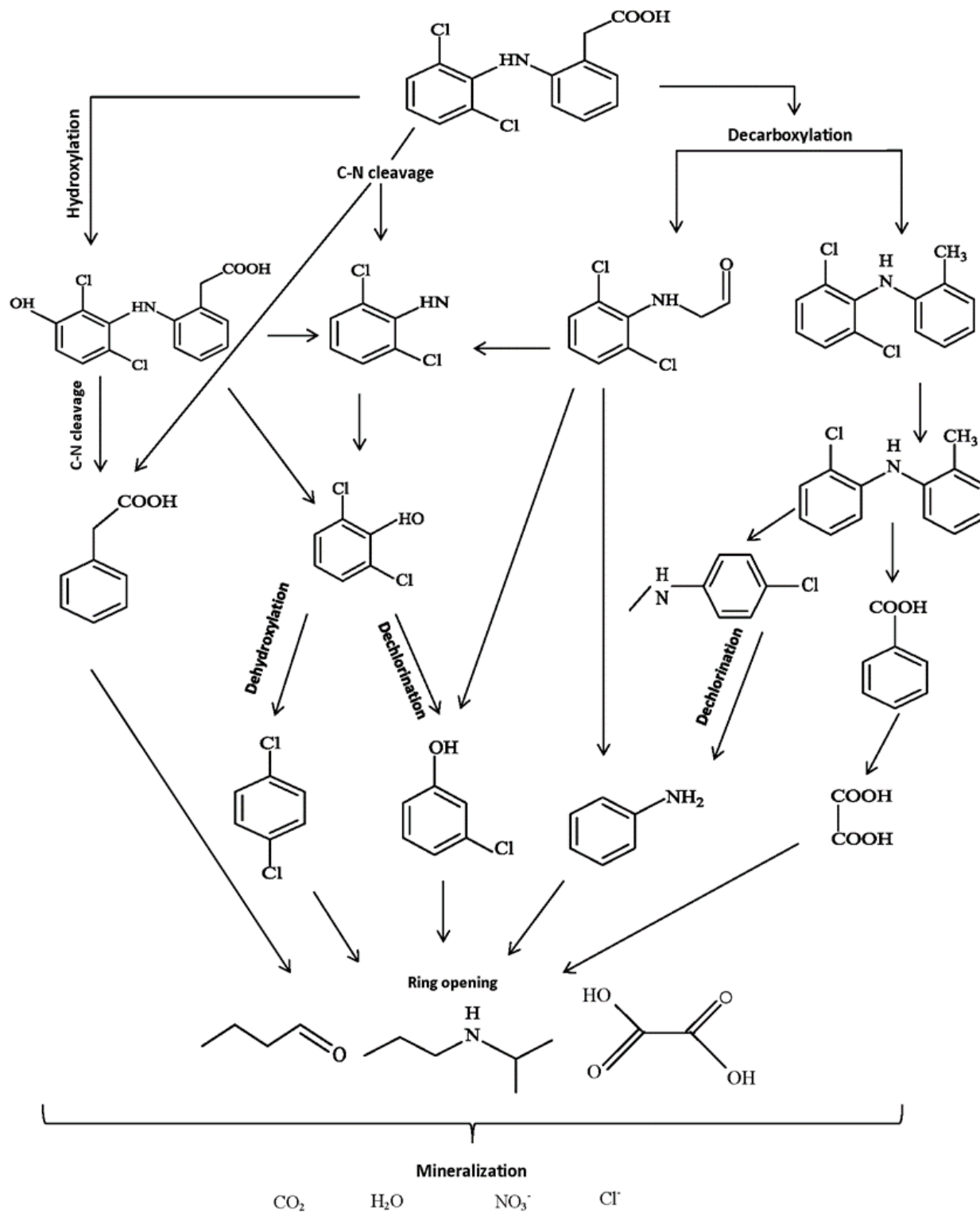
17	72.1	C ₄ H ₈ O		[M+ACN+H] ⁺	10
18	62	NO ₃ ⁻		[M+3Na] ⁺	10

19	35	Cl ⁻		[M+2K+H] ⁺	10

747

748 Based on Table 4, the linear carboxylic acids, carbon dioxide, chloride, and nitrate were identified in the
 749 reaction time of 10 min. The presence of aliphatic TPs, such as carboxylic acids, verified the high TOC
 750 removal obtained before (88%), i.e. DCF mineralization within 30 min reaction time. The identification
 751 of nitrate and chloride with m/z values of 62 and 35, respectively, referred to C-N and C-I bonds cleavages
 752 that reconfirmed the considerable mineralization efficiency through the oxidation mechanism (Moradi
 753 et al., 2020; Rao et al., 2018).

754



755

756

757

Fig. 10: The proposed pathway for DCF degradation in the HRS/PMS process

758 **4. Conclusions**

759 A naturally occurring ferruginous soil (Hormuz Red Soil-HRS) was characterized and used as a natural
760 material for PMS activation, aimed at developing an efficient AOP for degradation and mineralization of
761 an emerging water contaminant model, Diclofenac (DCF), and the inactivation of two model bacterial
762 contaminants, *E. coli* and *Enterococcus sp.* The catalytic potential of HRS under different conditions of
763 catalyst and oxidant concentrations, solution pH and water anions were evaluated, and in mild
764 operational conditions, namely low HRS catalyst loading and modest PMS concentrations, we report
765 effective disinfection and decontamination even in presence of high chloride or sulfate concentrations.
766 Scavenging experiments in conjunction with EPR measurements suggest a dominant radical pathway of
767 oxidation; a $\text{SO}_4^{\bullet-}$ based mechanism was found to be the dominant driving force in the efficient oxidation
768 and mineralization of DCF, with parallel contribution from $^1\text{O}_2$.

769 From the engineering point of view, HRS supported on alginate beads was prepared (HRSB), and its
770 potential and durability to activate PMS for the oxidation of DCF was confirmed over 5 catalytic cycles.
771 The HRSB/PMS process in a continuous flow packed bed reactor was examined, and complete
772 degradation of DCF was achieved at an HRT as low as 2 min. The LC/MS analysis of the effluent was
773 indicated that DCF was degraded into less toxic, simple and biodegradable by-products after treatment
774 by the developed process.

775 In conclusion, this work provided critical insights in the non-radical pathways of disinfection and
776 decontamination by PMS activation. Also, it is proven that HRS is an active, easily separable, and stable
777 natural catalyst to be used for efficient PMS activation, and the HRSB/PMS is deemed to be a cheap and
778 promising technology of continuous flow treatment for disinfection and decontamination of emerging
779 contaminants from water and wastewater streams.

780 **5. Acknowledgements**

781 This work was technically and financially supported by the Tarbiat Modares University, Iran, under the
782 Research Group grant No. IG-39801, and the Spanish Ministry of Science, Innovation and Universities via
783 PID2019-110441RB-C32 and PID2019-110441RB-C33 Projects). Also, Stefanos Giannakis would like to
784 acknowledge the Spanish Ministry of Science, Innovation and Universities (MICIU) for the Ramón y Cajal
785 Fellowship (RYC2018-024033-I).

786

787 **6. References**

- 788 1. Ma, H.-Y., Zhao, L., Guo, L.-H., Zhang, H., Chen, F.-J., Yu, W.-C. 2019. Roles of reactive oxygen species (ROS)
789 in the photocatalytic degradation of pentachlorophenol and its main toxic intermediates by TiO₂/UV.
790 *Journal of hazardous materials*, 369, 719-726.
- 791 2. Matzek, L.W., Carter, K.E. 2016. Activated persulfate for organic chemical degradation: a review.
792 *Chemosphere*, 151, 178-188.
- 793 3. Wang, J., Wang, S. 2018. Activation of persulfate (PS) and peroxymonosulfate (PMS) and application for
794 the degradation of emerging contaminants. *Chemical Engineering Journal*, 334, 1502-1517.
- 795 4. Li, Z., Liu, D., Zhao, Y., Li, S., Wei, X., Meng, F., Huang, W., Lei, Z. 2019. Singlet oxygen dominated
796 peroxymonosulfate activation by CuO-CeO₂ for organic pollutants degradation: performance and
797 mechanism. *Chemosphere*, 233, 549-558.
- 798 5. Zhou, X., Luo, C., Luo, M., Wang, Q., Wang, J., Liao, Z., Chen, Z., Chen, Z. 2020. Understanding the
799 synergetic effect from foreign metals in bimetallic oxides for PMS activation: a common strategy to
800 increase the stoichiometric efficiency of oxidants. *Chemical Engineering Journal*, 381, 122587.
- 801 6. Yan, J., Li, J., Peng, J., Zhang, H., Zhang, Y., Lai, B. 2019. Efficient degradation of sulfamethoxazole by the
802 CuO@Al₂O₃ (EPC) coupled PMS system: optimization, degradation pathways and toxicity evaluation.
803 *Chemical Engineering Journal*, 359, 1097-1110.
- 804 7. Liu, Y., Guo, H., Zhang, Y., Tang, W., Cheng, X., Li, W. 2018. Heterogeneous activation of
805 peroxymonosulfate by sillenite Bi₂₅FeO₄₀: singlet oxygen generation and degradation for aquatic
806 levofloxacin. *Chemical Engineering Journal*, 343, 128-137.
- 807 8. Cheng, X., Guo, H., Zhang, Y., Wu, X., Liu, Y. 2017. Non-photochemical production of singlet oxygen via
808 activation of persulfate by carbon nanotubes. *Water Research*, 113, 80-88.
- 809 9. Zhang, T., Chen, Y., Wang, Y., Le Roux, J., Yang, Y., Croué, J.P. 2014. Efficient peroxydisulfate activation
810 process not relying on sulfate radical generation for water pollutant degradation. *Environmental science
811 & technology*, 48, 5868-5875.
- 812 10. Yang, Q., Choi, H., Al-Abed, S.R., Dionysiou, D.D. 2009. Iron-cobalt mixed oxide nanocatalysts:
813 Heterogeneous peroxymonosulfate activation, cobalt leaching, and ferromagnetic properties for
814 environmental applications. *Applied Catalysis B: Environmental*, 88, 462-469.
- 815 11. Tian, X., Gao, P., Nie, Y., Yang, C., Zhou, Z., Li, Y., Wang, Y. 2017. A novel singlet oxygen involved
816 peroxymonosulfate activation mechanism for degradation of ofloxacin and phenol in water. *Chemical
817 Communications*, 53, 6589-6592.
- 818 12. Oh, W.D., Dong, Z., Hu, Z.T., Lim, T.T. 2015. A novel quasi-cubic CuFe₂O₄-Fe₂O₃ catalyst prepared at low
819 temperature for enhanced oxidation of bisphenol A via peroxymonosulfate activation. *Journal of
820 Materials Chemistry A*, 3, 22208-22217.
- 821 13. Deng, J., Xu, M., Qiu, C., Chen, Y., Ma, X., Gao, N., Li, X. 2018. Magnetic MnFe₂O₄ activated
822 peroxymonosulfate processes for degradation of bisphenol A: performance, mechanism and application
823 feasibility. *Applied Surface Science*, 459, 138-147.
- 824 14. Fu, H., Ma, S., Zhao, P., Xu, S., Zhan, S. 2019. Activation of peroxymonosulfate by graphitized hierarchical
825 porous biochar and MnFe₂O₄ magnetic nanoarchitecture for organic pollutants degradation: Structure
826 dependence and mechanism. *Chemical Engineering Journal*, 360, 157-170.
- 827 15. Ji, F., Li, C., Wei, X., Yu, J. 2013. Efficient performance of porous Fe₂O₃ in heterogeneous activation of
828 peroxymonosulfate for decolorization of Rhodamine B. *Chemical Engineering Journal*, 231, 434-440.
- 829 16. Jaafarzadeh, N., Ghanbari, F., Ahmadi, M. 2017. Catalytic degradation of 2, 4-dichlorophenoxyacetic acid
830 (2,4-D) by nano-Fe₂O₃ activated peroxymonosulfate: influential factors and mechanism determination.
831 *Chemosphere*, 169, 568-576.

- 832 17. Tan, C., Gao, N., Deng, Y., Deng, J., Zhou, S., Li, J., Xin, X. 2014. Radical induced degradation of
833 acetaminophen with Fe₃O₄ magnetic nanoparticles as heterogeneous activator of peroxymonosulfate.
834 *Journal of Hazardous Materials*, 276, 452-460.
- 835 18. Jawad, A., Zhan, K., Wang, H., Shahzad, A., Zeng, Z., Wang, J., Zhou, X., Ullah, H., Chen, Z. 2020. Tuning of
836 persulfate activation from a free radical to a nonradical pathway through the incorporation of non-redox
837 magnesium oxide. *Environmental Science and Technology*, 54, 2476-2488.
- 838 19. Zhang, X., Deng, H., Zhang, G., Yang, F., Yuan, G.-E. 2020. Natural bornite as an efficient and cost-effective
839 persulfate activator for degradation of tetracycline: Performance and mechanism. *Chemical Engineering
840 Journal*, 381, 122717.
- 841 20. Guan, G., Hao, X., Abudula, A. 2014. Heterogeneous Catalysts from natural sources for tar removal: a mini
842 review. *Journal of Advanced Catalysis Science and Technology*, 1, 20-28.
- 843 21. Demarchis, L., Minella, M., Nisticò, R., Maurino, V., Minero, C., Vione, D. 2015. Photo-Fenton reaction in
844 the presence of morphologically controlled hematite as iron source. *Journal of Photochemistry and
845 Photobiology A: Chemistry*, 307-308, 99-107.
- 846 22. Liang, X., Zhong, Y., Zhu, S., Zhu, J., Yuan, P., He, H., Zhang, J. 2010. The decolorization of Acid Orange II in
847 non-homogeneous Fenton reaction catalyzed by natural vanadium-titanium magnetite. *Journal of
848 Hazardous Materials*, 181, 112-120.
- 849 23. Xia, D., He, H., Liu, H., Wang, Y., Zhang, Q., Li, Y., Lu, A., He, C., Wong, P.K. 2018. Persulfate-mediated
850 catalytic and photocatalytic bacterial inactivation by magnetic natural ilmenite. *Applied Catalysis B:
851 Environmental*, 238, 70-81.
- 852 24. Su, S., Cao, C., Zhao, Y., Dionysiou, D.D. 2019. Efficient transformation and elimination of roxarsone and
853 its metabolites by a new α -FeOOH@GCA activating persulfate system under UV irradiation with
854 subsequent As (V) recovery. *Applied Catalysis B: Environmental*, 245, 207-219.
- 855 25. Chenxu, L., Zhendong, F., Jie, L., 2018. Water pollutants oxidation degradation through the activation of
856 peroxymonosulfate (PMS) heterogeneously catalyzed by transition metal oxide: a review. *Materials
857 Reports*, 32, 2223-2229.
- 858 26. Peng, J., Zhou, H., Liu, W., Ao, Z., Ji, H., Liu, Y., Su, S., Yao, G., Lai, B. 2020. Insights into heterogeneous
859 catalytic activation of peroxymonosulfate by natural chalcopyrite: pH-dependent radical generation,
860 degradation pathway and mechanism. *Chemical Engineering Journal*, 397, 125387.
- 861 27. Lai, L., Lai, B. 2020. Activation of peroxymonosulfate by natural molybdenite for the degradation of
862 atrazine, *E3S Web of Conferences*, 167, 01004.
- 863 28. Diao, Z.-H., Lin, Z.-Y., Chen, X.,-Z., Yan, L., Dong, F.-X., Qian, W., Kong, L.-J., Du, J.-J., Chu, W., 2020.
864 Ultrasound-assisted heterogeneous activation of peroxymonosulphate by natural pyrite for 2,4-
865 diclorophenol degradation in water: synergistic effects, pathway and mechanism. *Chemical Engineering
866 Journal*, 389, 123771.
- 867 29. Yan, S., Zhang, X., Shi, Y., Zhang, H. 2018. Natural Fe-bearing manganese ore facilitating bioelectro-
868 activation of peroxymonosulfate for bisphenol A oxidation, *Chemical Engineering Journal*, 354, 1120-1131.
- 869 30. Giannakis, S., Isabel, A., Gamo, M., Darakas, E., Escalas-Cañellas, A., Pulgarin, C. 2013. Impact of different
870 light intermittence regimes on bacteria during simulated solar treatment of secondary effluent:
871 Implications of the inserted dark periods. *Solar Energy*, 98, 572-581.
- 872 31. APHA 2017. *Standard methods for the examination of water and wastewater*, American Public Health
873 Association.
- 874 32. Gupta, P., De, A., Biswas, C. 2016. The effect of presence of SiO₂, Al₂O₃ and P₂O₅ on the reduction
875 behaviour of Fe₂O₃ nuggets with coke fines. *Arabian Journal for Science and Engineering*, 41, 4743-4752.
- 876 33. Zhang, C.-H., Wan, H.-J., Yang, Y., Xiang, H.-W., Li, Y.-W. 2006. Study on the iron-silica interaction of a co-
877 precipitated Fe/SiO₂ Fischer-Tropsch synthesis catalyst. *Catalysis Communications*, 7, 733-738.

- 878 34. Yu, X., Zhang, J., Wang, X., Ma, Q., Gao, X., Xia, H., Lai, X., Fan, S., Zhao, T.-S. 2018. Fischer-Tropsch
879 synthesis over methyl modified Fe₂O₃@SiO₂ catalysts with low CO₂ selectivity. *Applied Catalysis B:*
880 *Environmental*, 232, 420-428.
- 881 35. Lassoued, A., Dkhil, B., Gadri, A. & Ammar, S. 2017. Control of the shape and size of iron oxide (α -Fe₂O₃)
882 nanoparticles synthesized through the chemical precipitation method. *Results in Physics*, 7, 3007-3015.
- 883 36. Hu, Y., Wei, X., HU, Y., Wang, W., Fan, J., Liu, X., Chai, W., Zhou, Z., Ren, Z. 2019. Facile preparation of
884 sodium alginate-based gel spheres by droplet polymerization method for removal of levofloxacin from
885 aqueous solution. *Chemical Engineering Journal*, 123718.
- 886 37. Feng, J., Fan, D., et al. 2017. Facile synthesis silver nanoparticles on different xerogel supports as highly
887 efficient catalysts for the reduction of p-nitrophenol. *Colloids and Surfaces A: Physicochemical and*
888 *Engineering Aspects* 520: 743-756.
- 889 38. Naseri, A., Samadi, M. et al. 2017. Tuning composition of electrospun ZnO/CuO nanofibers: toward
890 controllable and efficient solar photocatalytic degradation of organic pollutants. *J. Phys. Chem. C* 121(6):
891 3327-3338.
- 892 39. Rahman, M.M., Asiri A.M. 2015. Development of ionic-sensor based on sono-chemically prepared low-
893 dimensional β -Fe₂O₃ nanoparticles onto flat-gold electrodes by an electrochemical approach. *Sensing and*
894 *Bio-Sensing Research* 4: 109-117.
- 895 40. Rao, Y., Han, F., Chen, Q., Wang, D., Xut, D., Wang, H., Pu, S. 2019. Efficient degradation of diclofenac by
896 LaFeO₃-Catalyzed peroxymonosulfate oxidation-kinetics and toxicity assessment. *Chemosphere*, 218, 299-
897 307.
- 898 41. Ahmed et al., 2012
- 899 42. Wu, M., Fu, K., Deng, H., Shi, J. 2019. Cobalt tetracarboxyl phthalocyanine-manganese octahedral
900 molecular sieve (OMS-2) as a heterogeneous catalyst of peroxymonosulfate for degradation of diclofenac.
901 *Chemosphere*, 219, 756-765.
- 902 43. Wu, M.H., Shi, J., Deng, H.P., 2018. Metal doped manganese oxide octahedral molecular sieve catalysts for
903 degradation of diclofenac in the presence of peroxymonosulfate. *Arabian Journal of Chemistry*, 11, 924-934.
- 904 44. Shao, H., Zhao, X., Wang, Y., Mao, R., Wang, Y., Qiao, M., Zhao, S., Zhu, Y. 2017. Synergetic activation of
905 peroxymonosulfate by Co₃O₄ modified g-C₃N₄ for enhanced degradation of diclofenac sodium under
906 visible light irradiation. *Applied Catalysis B: Environmental*, 218, 810-818.
- 907 45. Han, F., Ye, X., Chen, Q., Long, H. & Rao, Y. 2020. The oxidative degradation of diclofenac using the
908 activation of peroxymonosulfate by BiFeO₃ microspheres—kinetics, role of visible light and decay
909 pathways. *Separation and Purification Technology*, 232, 115967.
- 910 46. Othman, I., Zain, J.H., Haija, M.A., Banat, F. 2020. Catalytic activation of peroxymonosulfate using CeVO₄
911 for phenol degradation: an insight into the reaction pathway. *Applied Catalysis B: Environmental*, 118601.
- 912 47. Alahabadi, A., Moussavi, G. 2017. Preparation, characterization and atrazine adsorption potential of
913 mesoporous carbonate-induced activated biochar (CAB) from Calligonum Comosum biomass: Parametric
914 experiments and kinetics, equilibrium and thermodynamic modeling. *Journal of Molecular Liquids*, 242,
915 40-52.
- 916 48. Luo, R., Li, M., Wang, C., Zhng, M., Khan, M.A.N., Sun, X., Shen, J., Han, W., Wang, L., LI, J. 2019. Singlet
917 oxygen-dominated non-radical oxidation process for efficient degradation of bisphenol A under high
918 salinity condition. *Water Research*, 148, 416-424.
- 919 49. Rommozzi, E., Giannakis, S., Giovannetti, R., Vione, D., Pulgarin, C. 2020. Detrimental vs. beneficial
920 influence of ions during solar (SODIS) and photo-Fenton disinfection of E. coli in water: (Bi)carbonate,
921 chloride, nitrate and nitrite effects. *Applied Catalysis B: Environmental*, 270, 118877.
- 922 50. Li, Y., Li, J., Pan, Y., Xiong, Z., Yao, G., Xie, R., Lai, B. 2020. Peroxymonosulfate activation on FeCo₂S₄
923 modified g-C₃N₄ (FeCo₂S₄-CN): mechanism of singlet oxygen evolution for nonradical efficient degradation
924 of sulfamethoxazole. *Chemical Engineering Journal*, 384.

- 925 51. Wang, S., Tian, J., Wang, Q., Xiao, F., Gao, S., Shi, W., Cui, F., 2019. Development of CuO coated ceramic
926 hollow fiber membrane for peroxymonosulfate activation: a highly efficient singlet oxygen-dominated
927 oxidation process for bisphenol a degradation. *Applied Catalysis B: Environmental*, 256, 117783.
- 928 52. Kohantorabi, M., Giannakis, S., Gholami, M.R., Feng, L., Pulgarin, C., 2019. A systematic investigation on
929 the bactericidal transient species generated by photo-sensitization of natural organic matter (NOM)
930 during solar and photo-Fenton disinfection of surface waters. *Applied Catalysis B: Environmental*, 244,
931 983-995.
- 932 53. Serna-Galvis, E.A., Troyon, J.A., Giannakis, S., Torres-Palma, R.A., Minero, C., Vione, D., Pulgarin, C., 2018.
933 Photoinduced disinfection in sunlit natural waters: measurement of the second order inactivation rate
934 constants between *E. coli* and photogenerated transient species, *Water Research*, 147, 242-253.
- 935 54. Scully Jr., F.E., Hoigné, J. 1987. Rate constants for reactions of singlet oxygen with phenols and other
936 compounds in water. *Chemosphere*, 16, 681-694.
- 937 55. Xiao, R., Bai, L., Liu, K., Shi, Y., Minakata, D., Huang, C.-H., Spinney, R., Seth, R., Dionysiou, D.D., Wei, Z.,
938 Sun, P. 2020. Elucidating sulfate radical-mediated disinfection profiles and mechanisms of *Escherichia*
939 *coli* and *Enterococcus faecalis* in municipal wastewater. *Water Research*, 173, 115552.
- 940 56. Xiao, R., Liu, K., Bai, L., Minakata, D., Seo, Y., Göktaş, R.K., Dionysiou, D.D., Tang, C.-J., Wei, Z., Spinney, R.
941 2019. Inactivation of pathogenic microorganisms by sulfate radical: present and future. *Chemical*
942 *Engineering Journal*, 371, 222-232.
- 943 57. Yang, Y., Banerjee, G., Brudvig, G.W., Kim, J.-H., Pignatello, J.J., 2018. Oxidation of organic compounds in
944 water by unactivated peroxymonosulfate, *Environmental Science and Technology*, 2018, 52, 5911-5919.
- 945 58. Rodríguez-Chueca, J., Giannakis, S., Marjanovi, M., Kohantorabi, M., Gholami, M.R., Grandjean, D., de
946 Alencastro, L.F., Pulgarín, C. 2019. Solar-assisted bacterial disinfection and removal of contaminants
947 of emerging concern by Fe²⁺-activated HSO₅⁻ vs. S₂O₈²⁻ in drinking water, *Applied Catalysis B: Environmental*,
948 248, 62-72.
- 949 59. Deng, X., Li, S. 2018. Vapor phase synthesis of 2, 3, 6-trimethylphenol from m-cresol and methanol with
950 Fe₂O₃-SiO₂-CuO catalyst. *Catalysis Communications*, 111, 100-103.
- 951 60. Wei, R., Wang, P., Zhang, G., Wang, N., Zheng, T. 2019. Microwave-responsive catalysts for wastewater
952 treatment: a review. *Chemical Engineering Journal*, 122781.
- 953 61. Serna-Galvis, E.A., Troyon, J.A., Giannakis, S., Torres-Palma, R.A., Carena, L., Vione, D., Pulgarin, C., 2019.
954 Kinetic modeling of lag times during photo-induced inactivation of *E. coli* in sunlit surface waters:
955 unraveling the pathways of exogenous action, *Water Research*, 163, 114894.
- 956 62. Anipsitakis, G.P., Dionysiou, D.D. 2004. Radical generation by the interaction of transition metals with
957 common oxidants. *Environmental Science & Technology*, 38, 3705-3712.
- 958 63. Qi, C., Liu, X., Ma, J., Lin, C., Li, X., Zhang, H. 2016. Activation of peroxymonosulfate by base: implications
959 for the degradation of organic pollutants. *Chemosphere*, 151, 280-288.
- 960 64. Moradi, M., Moussavi, G., Yaghmaeian, K., Yazdanbakhsh, A., Srivastava, V., Sillanpää, M. 2020. Synthesis
961 of novel Ag-doped S-MgO nanosphere as an efficient UVA/LED-activated photocatalyst for non-radical
962 oxidation of diclofenac: catalyst preparation and characterization and photocatalytic mechanistic
963 evaluation. *Applied Catalysis B: Environmental*, 260, 118128.
- 964 65. Huang, Z., He, F., Zheng, A., Zhao, K., Chang, S., Zhao, Z., Li, H. 2013. Synthesis gas production from biomass
965 gasification using steam coupling with natural hematite as oxygen carrier. *Energy*, 53, 244-251.
- 966 66. Ahn, Y.-Y., Yun, E.-T., Seo, J.-W., Lee, C., Kim, S. H., Kim, J.-H., Lee, J. 2016. Activation of peroxymonosulfate
967 by surface-loaded noble metal nanoparticles for oxidative degradation of organic compounds.
968 *Environmental Science and Technology*, 50, 10187-10197.
- 969 67. Zheng, H., Bao, J., Huang, Y., Xiang, L., Ren, B., Du, J., Nadagouda, M.N., Dionysiou, D.D. 2019. Efficient
970 degradation of atrazine with porous sulfurized Fe₂O₃ as catalyst for peroxymonosulfate activation. *Applied*
971 *Catalysis B: Environmental*, 259, 118056.

- 972 68. Guo, S., Wang, H., Yang, W., Fida, H., You, L., Zhou, K. 2020. Scalable synthesis of Ca-doped α -Fe₂O₃ with
973 abundant oxygen vacancies for enhanced degradation of organic pollutants through peroxymonosulfate
974 activation. *Applied Catalysis B: Environmental*, 262, 118250.
- 975 69. Gao, P., Tian, X., Nie, Y., Yang, C., Zhou, Z., Wang, Y. 2019. Promoted peroxymonosulfate activation into
976 singlet oxygen over perovskite for ofloxacin degradation by controlling the oxygen defect concentration.
977 *Chemical Engineering Journal*, 359, 828-839.
- 978 70. Yang, S., Huang, Z., Wu, P., Li, Y., Dong, X., Li, C., Zhu, N., Duan, X., Dionysiou, D.D. 2020. Rapid removal of
979 tetrabromobisphenol A by α -Fe₂O_{3-x}@ Graphene@Montmorillonite catalyst with oxygen vacancies
980 through peroxymonosulfate activation: role of halogen and α -hydroxyalkyl radicals. *Applied Catalysis B:*
981 *Environmental*, 260, 118129.
- 982 71. Diaz-Urbe, C.E., Daza, M.C., Martínez, F., Páez-Mozo, E.A., Guedes, C.L.B., Mauro, E.D. 2010. Visible light
983 superoxide radical anion generation by tetra(4-carboxyphenyl)porphyrin/TiO₂: EPR characterization.
984 *Journal of Photochemistry and Photobiology A: Chemistry*, 215, 172-178.
- 985 72. Chen, Z., Bi, S., Zhao, G., Chen, Y., Hu, Y. 2019. Enhanced degradation of triclosan by cobalt manganese
986 spinel-type oxide activated peroxymonosulfate oxidation process via sulfate radicals and singlet oxygen:
987 Mechanisms and intermediates identification. *Science of The Total Environment*, 134715.
- 988 73. Nihemaiti, M., Miklos, D.B., Hubner, U., Linden, K.G., Drewes, J.E., Croue, J.-P. 2018. Removal of trace
989 organic chemicals in wastewater effluent by UV/H₂O₂ and UV/PDS. *Water Research*, 145, 487-497.
- 990
991